

ABSTRACT

Title of Dissertation: **BIOMIMETIC NANOSTRUCTURES FOR
THERANOSTIC APPLICATIONS**

Yuan-Chia Kuo, Doctor of Philosophy, 2015

Dissertation directed By: Professor Warren D. D'Souza
Department of Bioengineering

Professor Srinivasa R. Raghavan
Department of Chemical and Biomolecular Engineering

Theranostic nanostructures are those that have both therapeutic as well as diagnostic function, e.g., due to having a combination of drugs as well as imaging agents in them. Such structures, especially those that can selectively home in on cancer tumors, have received considerable attention recently. Although many different structures have been synthesized, their complexity, high cost, and poor biocompatibility have limited their clinical application. In this study, we focus on creating new classes of theranostic nanostructures using simple routes (via self-assembly) and utilizing inexpensive and biocompatible materials.

In our first study, we describe a class of liposomal probes that can allow certain tumors to be imaged by magnetic resonance imaging (MRI). Tumors, such as those of

head and neck cancer, are known to over-express the epidermal growth factor receptor (EGFR). Our liposomal probes bear anti-EGFR antibodies as well as chelated gadolinium (Gd), a positive (image-brightening) contrast agent for MRI. To synthesize these probes, we use a strategy that is carefully designed to be simple and scalable: it employs two steps that each involve self-assembly. The resulting probes bind *in vitro* to EGFR-overexpressing tumor cells compared to controls. Moreover, cancer cells with bound probes can be tracked by MRI. In the future, these probes could find clinical use for tracking the efficacy of cancer treatment in real-time.

Next, we report a class of microscale (3 to 5 μm) containers derived from erythrocytes (red blood cells). Micro-erythroosomes (MERs) are produced by emptying the inner contents of these cells and resuspending the empty structures in buffer. We have developed procedures to functionalize the surfaces of the MERs with targeting moieties (such as anti-EGFR antibodies) and also to load solutes (such as fluorescent dyes and MRI contrast agents) into the cores of the MERs. Thus, we show that MERs are a versatile class of microparticles for biomedical applications.

In our final study, we show that the MERs from the previous study can be sonicated to yield nanoscale structures, termed nano-erythroosomes (NERs), with average sizes around 120 nm. NERs are membrane-covered nanoscale containers, much like liposomes. They show excellent colloidal stability in both buffer as well as in serum, and they are able to withstand freeze-thaw cycling. Moreover, NER membranes can be decorated with fluorescent markers and antibodies, solutes can be encapsulated in the cores of the NERs, and NERs can be targeted towards mammalian cells. Thus, NERs are a promising and versatile class of nanostructures for use in nanomedicine.

BIOMIMETIC NANOSTRUCTURES FOR THERANOSTIC APPLICATIONS

By

Yuan-Chia Kuo

Dissertation submitted to the Faculty of the Graduate School of the
University of Maryland, College Park, in partial fulfillment
of the requirements for the degree of
Doctor of Philosophy
2015

Advisory Committee:

Prof. Warren D. D'Souza, Dept. of Bioengineering, Chair

Prof. Srinivasa R. Raghavan, Dept. of Chemical & Biomolecular Engineering, Co-chair

Prof. William E. Bentley, Dept. of Bioengineering

Prof. Yu Chen, Dept. of Bioengineering

Prof. Ian White, Dept. of Bioengineering

Prof. Don L. DeVoe, Dept. of Mechanical Engineering

© Copyright by
Yuan-Chia Kuo
2015

Dedication

This dissertation is dedicated to my beloved father. Without him, this journey would not have been possible. Being a business man, he always feels the knowledge is important than everything. As a result, I have been suggested to pursue the highest degree in biomedical science in order to improve the life of human beings. The story will not stop here, and I will keep following his advice to make as much contributions as I can. It is with pride and affection that I dedicate this dissertation to my father,

Kuo, Yi-Hsiung
(1938-2005)

Acknowledgements

First, I would like to thank both of my advisors Dr. Warren D'Souza, and Dr. Srinivasa Raghavan for their unwavering support regardless of the research conducted, I am fortunate to have them guiding me in this fantastic scientific realm without losing direction. They have been a positive influence from my first day in lab to my graduation. They inspired me to strive to continually improve myself, whilst patiently correcting my writing and financially supporting my research. Furthermore, they encouraged me to broaden my view and gave me a plethora of suggestions for my tenure as a graduate student. This work wouldn't have been possible without them; therefore, when I am successful in my career, credit needs to be attributed to my mentors.

I would like to thank my committee members: Dr. William Bentley, Dr. Yu Chen, Dr. Ian White, Dr. Greg Payne, and Dr. Don DeVoe for their guidance and support during my proposal and dissertation. I would specifically like to thank Dr. William Bentley for his assistance in finding a lab during my first year, and for the collaboration with his lab.

As for the collaboration, I would especially express my thanks to my first teacher here, Dr. Chiwei Hung, who shared his lab space as well as his wealth of experience with me. I would also like to thank, Dr. Chen-Yu Tsao, Dr. David Quan, Dr. Hsuan-Chen Wu for their wonderful mentorship, and I am glad that I had them at my side during difficult times. Almost no technical or life issues can cause any major setbacks for them as they are extremely knowledgeable, thoughtful and reliable. In addition, my research would not have been possible without their assistance and guidance.

I am glad that I joined the Complex Fluids group, and I owe a debt of gratitude to previous and current colleagues who have positively influenced my graduate life at UMD: Matt Dowling, Hee-Young Lee, Hyuntaek Oh, Annie Lu, Vishal Javvaji, Kunqiang Jiang, Jasmin Athas, Ankit Gargava, Dao Hoang, Kunal Pandit, Bani Cipriano, Peter Thomas, Stephen Banik, Brady Zarket, Ian MacIntire, Salimeh Gharazi, Joe White, Veidhes Basrur, Anand Bagal, Chanda Arya, Kevin Diehn, Ankit Goyal, and Veena Rao. It's been a pleasure to work with them, and it would have been a lonely lab without them.

To my dear friends and my class at Maryland, thank you for accompanying me whether it be for delicious food, traveling, exercise and shopping.

I want to express a deep heartfelt thanks to my girlfriend, Shuchun Wang, who cheered me up and stood by me through the good times and bad. Without her support and company, life would not have been so exciting and joyful.

Last, I would like to thank my dad, who always supported my graduate studies and seriously considered my study abroad even during his last moments. I am sure he would have been really proud of me. My mom has also fully supported me while she pursues a Chinese medicine doctorate degree in China, and I hope she can do well in her exams to achieve her dream of becoming a doctor. To my elder brothers, nephews and nieces, thank you for taking care everything during my absence from home. You are the best family I can have.

Table of Contents

Dedication	ii
Acknowledgements	iii
Table of Contents	v
List of Tables	vii
List of Figures	viii
Chapter 1: Introduction and Overview	1
1.1. Problem Description and Motivation.....	1
1.2. Proposed Approach.....	3
1.2.1. Liposomes.....	3
1.2.2. Micro-Erythroosomes (MERs).....	4
1.2.3. Nano-Erythroosomes (NERs).....	4
1.3. Significance of This Work.....	5
Chapter 2: Background	6
2.1. Tumor Targeting via EGFR.....	6
2.2. Imaging Techniques during Cancer Treatment.....	8
2.3. Magnetic Resonance Imaging (MRI).....	9
2.4. Vesicles and Liposomes.....	12
2.5. Dynamic Light Scattering (DLS).....	15
Chapter 3: Liposomes as Theranostic Nanoprobes	17
3.1. Introduction.....	17

3.2. Experimental Section	20
3.3. Results and Discussion	25
3.4. Conclusions.....	38
Chapter 4: Micro-Erythroosomes and Their Colloidal Properties.....	39
4.1. Introduction.....	39
4.2. Experimental Section.....	40
4.3. Results and Discussion	43
4.4. Conclusions.....	54
Chapter 5: Nano-Erythroosomes and Their Colloidal Properties	55
5.1. Introduction.....	55
5.2. Experimental Section.....	57
5.3. Results and Discussion	63
5.4. Conclusions.....	78
Chapter 6: Conclusions and Recommendations	79
6.1. Project Summary and Principal Contributions	79
6.2. Recommendations for Future Work.....	81
Chapter 7: References	84

List of Tables

Table 2.1. Summary of current imaging technologies.....	9
--	---

List of Figures

- Figure 2.1.** Schematic illustration of EGFR mediated signal transduction. The activation of EGFR by its ligand or by irradiation may cause the signal transduction cascade which affected the cell metabolism, gene expression, proliferation and survival.....7
- Figure 2.2.** Basic description of magnetic resonance imaging (MRI): (a) to (e). A T₁ weighted image is shown in (f).....10
- Figure 2.3.** Schematics depicting the connection between the geometry of amphiphilic molecules and the structures they form in water. The hydrophilic heads of the amphiphiles are shown in blue and the hydrophobic tails in red.....14
- Figure 3.1.** Structure of CAGE probes with Chelated Gd and antibodies to EGFR within a single structure of size ~ 100 nm. (Top) The lipids DPPC, Cholesterol, Gd-DTPA-bSA, DOPE-mPEG, and DOPE-biotin are combined to produce Gd-liposomes. (Bottom) The Gd-liposomes are combined with biotinylated *Cetuximab* (anti-EGFR antibody) and the tetrafunctional protein, avidin. The antibodies get attached to the Gd-liposomes via biotin-avidin interactions to form the CAGE probe. “CAGE” includes chelated Gd and antibodies to EGFR.....20
- Figure 3.2.** Liposome size and stability over a period of 18 days. Data are shown for Gd-liposomes (no antibody) and for the CAGE probes (liposomes with antibody attached). The sizes correspond to the hydrodynamic diameters from DLS.....27
- Figure 3.3.** TEM images of liposome structures stained with 1% uranyl acetate. (a,b) Gd-liposomes; (c,d) CAGE probes.....29
- Figure 3.4.** Relaxivity plots of $1/T_1$ vs. Gd^{3+} from MR measurements. Plots are shown for solutions of Gd-DTPA as well as for solutions containing Gd-liposomes. The slopes of the lines give the relaxivities for each sample (Gd-liposomes: $r_1 = 8.07 \text{ mM}^{-1}\text{s}^{-1}$, CAGE Probe: $r_1 = 3.93 \text{ mM}^{-1}\text{s}^{-1}$ and Gd-DTPA: $r_1 = 3.3 \text{ mM}^{-1}\text{s}^{-1}$).....30
- Figure 3.5.** EGFR expression of normal HEK cells compared with that of SCCHN 15B cells by flow cytometry and fluorescence microscopy. (a) Very low Alexa Fluor fluorescence signal (green) is observed with HEK cells (2.79%) which implies low levels of EGFR expression. (b) In comparison, a high Alexa Fluor signal is found for 15B cells (99.8%). Note that in the micrographs, the cell nucleus stained by DAPI gives blue fluorescence, while the Alexa Fluor-bound antibody gives green fluorescence.....31
- Figure 3.6.** Cell viability (MTT) assay of 15B cells incubated with different structures. Gd-liposomes show low toxicity to cells, while the CAGE probes are somewhat toxic above 2 mg/mL.....33
- Figure 3.7.** EGFR-mediated binding of Gd-liposomes and CAGE probes by HEK and 15B cells. Since the Gd-liposomes do not have any targeting function, they show some non-specific binding to both HEK cells (a) and 15B cells (b). On the other hand, the

CAGE probes are able to bind significantly more to EGFR-overexpressing 15B cells (d) compared to HEK cells (c).....34

Figure 3.8. Competition assay of CAGE probes (red) with the sc-120 AF488 EGFR antibody (green) for evaluation of specific binding affinity in 15B cells. (a) 1:50 sc-120 alone (b) 1:50 sc-120, 0.1 mg/mL of CAGE, (c) 1:50 sc-120, 0.8 mg/mL of CAGE, (d) 1:50 sc-120, 2 mg/mL of CAGE.....36

Figure 3.9. MRI screening of CAGE probe-targeted 15B cells. T₁ values and MR images at TI =1000 ms for pure water, 0.5 mM Gd-DTPA, Gd-liposome and CAGE probe-targeted 15B cells. T₁ values were calculated based on the intensity inside the circle by adapting a curve fitting tool in Matlab.....37

Figure 4.1. Preparation of MERs from bovine whole blood. Red cells were separated, burst via hypotonic PBS to cause hemoglobin release, and purified via ultracentrifugation to remove the hemoglobin in the supernatant. Unlysed MERs are in the bottom pellet. The MERs were then functionalized with antibody using biotin-avidin linkages.....43

Figure 4.2. Stability of erythroosomes. a) ERs in PBS over a period of two weeks. b) Zetapotential of ERs is about -30 ~ -40 mV.....44

Figure 4.3. Decoration of MERs with fluorescent lipids. The figure is a superimposition of green and red fluorescence from a sample containing a 1:1 mixture of MERs with the red fluorescent lipid DiI and MERs with the green fluorescent lipid DiO. The structures are suspended in water (hypotonic solution), and hence are swollen into spheres.....46

Figure 4.4. Surface modification of MERs by biotin-avidin interactions. (a) MERs with DiI and DOPE-Biotin show red fluorescence. (b) To this, when avidin-FITC is added, we see green fluorescence at the same spots, indicating binding of avidin to the biotins on the MERs. (c) A superimposed image of green and red fluorescence confirms this binding.....47

Figure 4.5. Imparting magnetic properties to MERs. This is done by binding streptavidin-coated magnetic beads to MERs with DiI and biotin. The images are stills from a movie, in order from a to d. The arrows indicate the motion of MERs at different time points.....48

Figure 4.6. Encapsulation of dextran-FITC in various structures. The images on the left are bright field views while those on the right are for green fluorescence. (a) and (b) sealed RBCs; (c) and (d) unsealed ERs; (e) and (f) sealed ERs.....50

Figure 4.7. Release of Gd-DTPA from MERs. Data are shown for two different sealing times.....52

Figure 4.8. Targeted binding of MERs with 15B cells (which overexpress EGFRs). (a) MERs alone, (b) MERs with biotin, c) MERs with anti-EGFR antibodies. The blue

fluorescence represents the DAPI nucleus counterstain, and the red fluorescence comes from the DiI on the MERs.....53

Figure 5.1. Preparation of ERs and NERs from bovine whole blood. Red cells were a) separated, burst via hypotonic PBS to cause hemoglobin release, and b) purified via ultracentrifugation to remove the hemoglobin in the supernatant. c) Unlysed ERs are in the bottom pellet. d) The NERs were prepared from transparent ERs via sonication.....64

Figure 5.2. Sizes (hydrodynamic diameters from DLS) of NERs over a period of two weeks in water (circles) and in PBS (squares). NERs in PBS show a bluish tint.....65

Figure 5.3. Cryo-TEM images of NERs. a) In isotonic solution, most NERs are unilamellar vesicles with sizes around 100 nm. In rare cases, NERs may also have two concentric membranes (b), or vesicle-in-vesicle structures: (c) and (d). NERs in hypertonic solution appear as biconcave structures: (e) and (f).....67

Figure 5.4. SANS spectra for NERs in D₂O. The intensity *I* follows a slope of -2 at low *q*, which is characteristic of unilamellar vesicles.....69

Figure 5.5. (a) Stability of NERs compared to liposomes or PEG-conjugated liposomes. (a) in serum; (b) in buffer, following freeze/thaw cycling. Filled points in (b) imply that the sample showed a precipitate.72

Figure 5.6. Release of solute (dextran-FITC) encapsulated in NERs or liposomes. The samples were placed in dialysis cassettes. The samples were dialyzed against excess of PBS buffer for more than four days at room temperature with constant stirring and buffer exchanges. Aliquots were withdrawn from the dialysis bag at various time points and analyzed for the concentration of solute.....74

Figure 5.7. Attachment of targeting moieties to NERs, and evaluation of their targeting affinity. (Top) Schematic of mTG-mediated conjugation of protein G via glutamine to lysine on NERs, followed by spontaneous binding of protein G to the stem of antibodies. (Bottom) Fluorescence micrographs of 15B cells (which overexpress EGFR) incubated with a) blank, b) liposomes, c) NERs with protein G-IgG_{2a}, d) NERs with protein G-anti-EGFR. Green represents cell boundaries, blue is DAPI counterstain of nuclei, and red indicates the nanostructures.....76

Figure 6.1. Structures of phospholipid and derivative. One acyl chain is removed from phospholipid by phospholipase and generates lysophospholipid.....81

Figure 6.2. Glucose oxidase commonly used on food market. a) Glucose oxidase can convert glucose into gluconic acid and hydrogen peroxide, b) once the targeted MERs attach to the surface of cells, then the product of enzyme may kill cells by hydrogen peroxide.....82

Chapter 1

Introduction and Overview

1.1. Problem Description and Motivation

This dissertation is devoted to the development of “theranostic” nanostructures. The term “theranostic” is a combination of the words “therapeutic” and “diagnostic”. It thus refers to nanostructures that can have therapeutic function, i.e., in treating diseases like cancer, as well as diagnostic capabilities, i.e., in analyzing the presence or extent of the disease. Current research in nanomedicine is increasingly focusing on such types of multifunctional agents, and the work done here is a step in that direction.

Development of nanoscale therapeutics with specificity for targeting cancerous cells without harming normal tissues is of great significance in cancer treatment. Such therapeutics provide new directions and hope for eradicating tumors. To optimize the efficacy of therapeutic efforts, it is advantageous to monitor the progression of the disease in real time. This is where diagnostic agents and imaging techniques come into play. Computed tomography (CT), positron emission tomography (PET), and magnetic resonance imaging (MRI) are the most useful live imaging technologies for cancer evaluation.¹ Among these methods, MRI is emerging as a preferred imaging technique. MRI is advantageous in that it provides high-resolution details and better contrast for discriminating between normal and tumor tissue, especially when used in conjunction with contrast agents.

Contrast agents for MRI fall into two categories: negative-contrast (image-darkening) agents like iron oxide and positive-contrast (image-brightening) agents, such as gadolinium (Gd). Negative-contrast agents yield dark signals on images, often making it difficult to differentiate the tumor from air passages in images. In comparison, positive-contrast agents like Gd^{3+} produce signal enhancement. Gd^{3+} is a paramagnetic ion that shortens the T_1 and T_2 relaxation times of nearby water protons, thereby providing an increased signal on the MR image.²⁻⁴ Because Gd^{3+} is toxic, it is often used in the clinic in a chelated form, where the cation is bound to a cage-like anion.

An example of a theranostic nanoparticle for cancer treatment is one that has the following constituents: (a) therapeutic drugs in the particle core or attached to its surface; (b) diagnostic moieties like chelated gadolinium, either in the core or attached to its surface; and (c) a targeting moiety to allow the particle to home in to the site of the tumor. Such a particle would potentially accumulate at the site of the tumor and deliver its payload (drugs), while at the same time allowing the tumor to be visualized by MRI.

While the potential for nanoparticles in cancer treatment is enormous, currently there are very few examples of these particles being used by doctors in the clinic. There are many reasons for this, including the fact that these particles are very costly and difficult to prepare, often exhibit limited stability under long-term storage, and also exhibit rather high levels of toxicity to humans. The long-term motivation for our work is to put forward new kinds of nanoparticles that can address some of the above concerns and thereby emerge as viable candidates for eventual clinical applications.

1.2. Proposed Approach

In this dissertation, we will describe three classes of nanoparticles that have potential for theranostic applications. Each of these nanoparticles has a lipid membrane surrounding an aqueous core; thus, each of them resembles the structure of a biological cell. Importantly, the nanoparticles are assembled and held together as a result of non-covalent (weak) interactions rather than by covalent bonds: this process is termed “self-assembly”. We believe that such self-assembled nanoparticles made from lipids can be relatively cost-effective, easy to prepare, and exhibit a high degree of biocompatibility (low toxicity). Therefore, the particles can be attractive candidates for eventual use in the clinic. The three classes of nanoparticles are described in further detail below.

1.2.1. Liposomes

First, in Chapter 3, we describe a class of liposomes conjugated with chelated Gd as well as antibodies to the epidermal growth factor receptor (EGFR). EGFRs are known to be overexpressed on the membranes of certain tumors. Therefore, anti-EGFR antibodies serve as targeting agents and allow the liposomes to home in to the locations of tumors. In addition, these antibodies also have a therapeutic effect because their binding to the cells eliminates downstream signaling pathways and thereby slows or eliminates the proliferation of the cancer. The presence of Gd on the liposomes also allows the tumor to be imaged using MRI. Thus, the liposomes in this study serve as theranostic agents. A notable feature of our synthesis method in this study lies in its simplicity. We use self-assembly to conjugate the Gd and antibody to the liposome,

unlike previous studies that have required various chemical reactions to perform such conjugation. Thus, our approach is simple, biocompatible, and one that will scale easily.

1.2.2. Micro-Erythroosomes (MERs)

In Chapter 4, we focus on micro-sized particles derived from erythrocytes or red blood cells (RBCs). These are termed micro-erythroosomes (MERs) with sizes ranging from 3 to 5 μm , and they are produced by emptying the inner contents of RBCs (specifically hemoglobin) and resuspending the empty structures in buffer. Although the ability to form MERs has been known for decades, very little is known about these structures, and they currently find limited use. We have developed a systematic procedure to convert RBCs into MERs and furthermore to functionalize the surfaces of the MERs with targeting moieties, including anti-EGFR antibodies. We have also developed a strategy to load solutes (such as fluorescent dyes and MRI contrast agents) into the cores of the MERs, which can subsequently be delivered across the MER membrane. Thus, we show that MERs can be a class of particles that are biocompatible, inexpensive, and easy to prepare and optimize for applications.

1.2.3. Nano-Erythroosomes (NERs)

In Chapter 5, we further expand on the erythroosome system from Chapter 4. Because the MERs are microscale structures, they are too large to enter mammalian cells. We have found that, by shearing the MERs, we can reduce their size to the nanoscale (~ 100 nm), thereby generating nano-erythroosomes (NERs). The NERs are analogous to the liposomes from Chapter 3, although very little is known about them in the literature.

Here, for the first time, we undertake a systematic study into their colloidal properties. We find that NERs are very stable to aggregation or fusion compared to conventional liposomes, and are able to withstand freeze-thaw cycling. Moreover, much like conventional liposomes, drugs can be encapsulated in the cores of NERs, and NER membranes can be decorated with fluorescent markers or with anti-EGFR antibodies. Thus, NERs are a promising and versatile class of particles for use in nanomedicine.

1.3. Significance of This Work

The significance of this work is that it presents new, alternative classes of theranostic structures. Our focus is on preparing biocompatible structures using simple and inexpensive synthesis routes, and starting from readily available precursors. We use self-assembly rather than covalent chemical bonding to functionalize these structures with antibodies or other moieties. Because of the simplicity involved, the structures described here are potentially easier to make at large scales, and this should make them attractive for future applications.

Also, the MERs and NERs (Chapters 4, 5) are an interesting direction that is new and different. Our studies have been conducted with bovine blood, but we envision these being extended to human blood. Thus, there is the potential for extracting blood from a patient and using it to make MERs and NERs, which will be entirely compatible with the patient without eliciting any immune response or adverse effects. Such nanostructures could be re-injected into the patient as theranostic agents, e.g., to track or treat cancer cells. This concept could prove important in the future.

Chapter 2

Background

This dissertation is concerned with self-assembled theranostic particles that can deliver payloads to target cells. Cancer cells that overexpress markers on their surfaces can be targeted using antibodies to these markers. In this chapter, we will review the basics of cancer targeting, the fundamentals of imaging techniques, specifically MRI, the basics of forming self-assembled particles from lipids, and a few of the characterization techniques used in this work.

2.1. Tumor Targeting via EGFR

Scientists have been increasingly looking for ways to attack malfunctioned cancer cells without damaging normal cells, thus reducing the side effects during cancer therapy. For this, it is important to target the molecules specifically present on/in tumor cells, such as components responsible for tumorigenic signaling, rapid cell proliferation, angiogenesis, DNA repair, and cell migration. Once such molecules have been identified, monoclonal antibodies against the molecule become a powerful tool for tumor identification.

In this regard, one signature of various human cancers such as those of the brain, head and neck, lung, thyroid, colon, kidney, prostate, ovarian, bladder, and breast, is over-expression of the epidermal growth factor receptor (EGFR).⁵ Increased abundance of EGFR results in constitutive activation of EGFR signaling and is often related with tumor

resistance toward chemotherapy and radiotherapy. Also, EGFR signaling activated by its conventional ligands (e.g., EGF and TGF- α) or by ionizing radiation promotes cell proliferation, migration, and angiogenesis, thus potentiating the metastatic risk and poor prognosis of these cancers (Figure 2.1).⁶

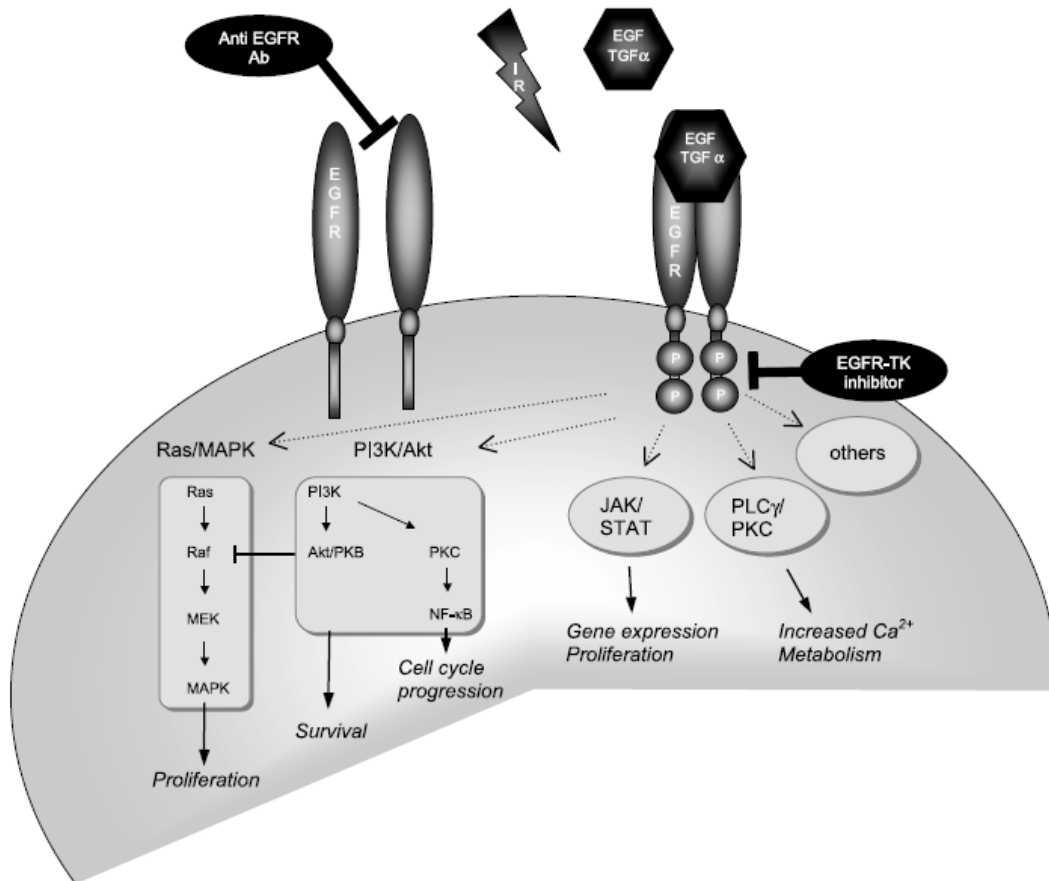


Figure 2.1. Schematic illustration of EGFR mediated signal transduction. The activation of EGFR by its ligand or by irradiation may cause the signal transduction cascade which affected the cell metabolism, gene expression, proliferation and survival.¹

Recently, anti-EGFR monoclonal antibodies have been developed. These have been shown to have a direct therapeutic effect. For example, incubation of these antibodies with carcinoma cell lines derived from colon, breast, head and neck, stomach,

prostate, and kidney cancers successfully prevented cell growth and invasion.⁷ The mechanism of this anti-tumor effect is believed to be through the blocking of intracellular EGFR signaling. Accordingly, certain FDA-approved EGFR-targeting monoclonal antibodies are now used directly in the clinic for cancer treatment.

One FDA-approved anti-EGFR antibody is Cetuximab, which is used to treat squamous cell carcinoma of the head and neck (SCCHN). Cetuximab is an engineered mouse/human chimeric antibody. Results from *in vitro* and animal studies have shown that Cetuximab can augment the effects of radiation and chemotherapeutics with increased tumor apoptosis and reduced tumor burdens.⁸ Clinical trials also have demonstrated that Cetuximab in combination with radiotherapy improves the 5-year overall survival rate of SCCHN patients to 46%, compared with 36% of the radiotherapy-alone group.⁹ When combined with chemotherapy, Cetuximab lengthened the median overall survival from 7.4 to 10.1 months.¹⁰ The recommended administration schedule of Cetuximab for SCCHN treatment is 400 mg/m² as an initial induction dose followed by 250 mg/m² as a weekly dose for a 7-week duration.

2.2. Imaging Techniques during Cancer Treatment

To trace the progression of cancer therapy *in vivo*, imaging techniques provide a viable approach. Table 2.1 compares a wide range of imaging techniques. Fluorescence imaging is a widely used method in molecular biology; however, its low resolution and short penetration depth (< 1 cm) preclude its use for cancer monitoring. These limitations are also applicable for bio-luminescence.¹ Computed tomography (CT), positron

emission tomography (PET), and magnetic resonance imaging (MRI) are the most useful imaging technologies for cancer. They allow for quantitative imaging.

Table 1 Overview of imaging systems										
Technique	Resolution*	Depth	Time†	Quantitative‡	Multi-channel	Imaging agents	Target	Cost*\$	Main small-animal use	Clinical use
MRI	10–100 μm	No limit	Minutes to hours	Yes	No	Paramagnetic chelates, magnetic particles	Anatomical, physiological, molecular	\$\$\$	Versatile imaging modality with high soft-tissue contrast	Yes
CT	50 μm	No limit	Minutes	Yes	No	Iodinated molecules	Anatomical, physiological	\$\$	Imaging lungs and bone	Yes
Ultrasound	50 μm	cm	Seconds to minutes	Yes	No	Microbubbles	Anatomical, physiological	\$\$	Vascular and interventional imaging	Yes
PET	1–2 mm	No limit	Minutes to hours	Yes	No	^{18}F -, ^{64}Cu - or ^{11}C -labelled compounds	Physiological, molecular	\$\$\$	Versatile imaging modality with many tracers	Yes
SPECT	1–2 mm	No limit	Minutes to hours	Yes	No	$^{99\text{m}}\text{Tc}$ - or ^{111}In -labelled compounds	Physiological, molecular	\$\$	Imaging labelled antibodies, proteins and peptides	Yes
Fluorescence reflectance imaging	2–3 mm	<1 cm	Seconds to minutes	No	Yes	Photoproteins, fluorochromes	Physiological, molecular	\$	Rapid screening of molecular events in surface-based disease	Yes
FMT	1 mm	<10 cm	Minutes to hours	Yes	Yes	Near-infrared fluorochromes	Physiological, molecular	\$\$	Quantitative imaging of fluorochrome reporters	In development
Bioluminescence imaging	Several mm	cm	Minutes	No	Yes	Luciferins	Molecular	\$\$	Gene expression, cell and bacterium tracking	No
Intravital microscopy¶	1 μm	<400–800 μm	Seconds to hours	No	Yes	Photoproteins, fluorochromes	Anatomical, physiological, molecular	\$\$\$	All of the above at higher resolutions but limited depths and coverage	In development#

Table 2.1. Summary of current imaging technologies. ⁴

2.3. Magnetic Resonance Imaging (MRI)

MRI is an imaging modality that uses a magnetic field and non-ionizing radiation at radio frequencies (RF) to create an image of the regions of interest, particularly of abnormalities in soft tissue. Compared to other imaging methods, MRI has the following advantages: (1) better tissue contrast for discriminating normal and tumor tissue (with the assistance of contrast agents), (2) higher sensitivity in detecting metastatic tumors such as bone, liver, and lung, and (3) lack of exposure to X-rays, thus, being less damaging to patients who need repeated examination and screening.¹¹ MRI can potentially reveal high-resolution anatomical differences between tumors and normal tissues.

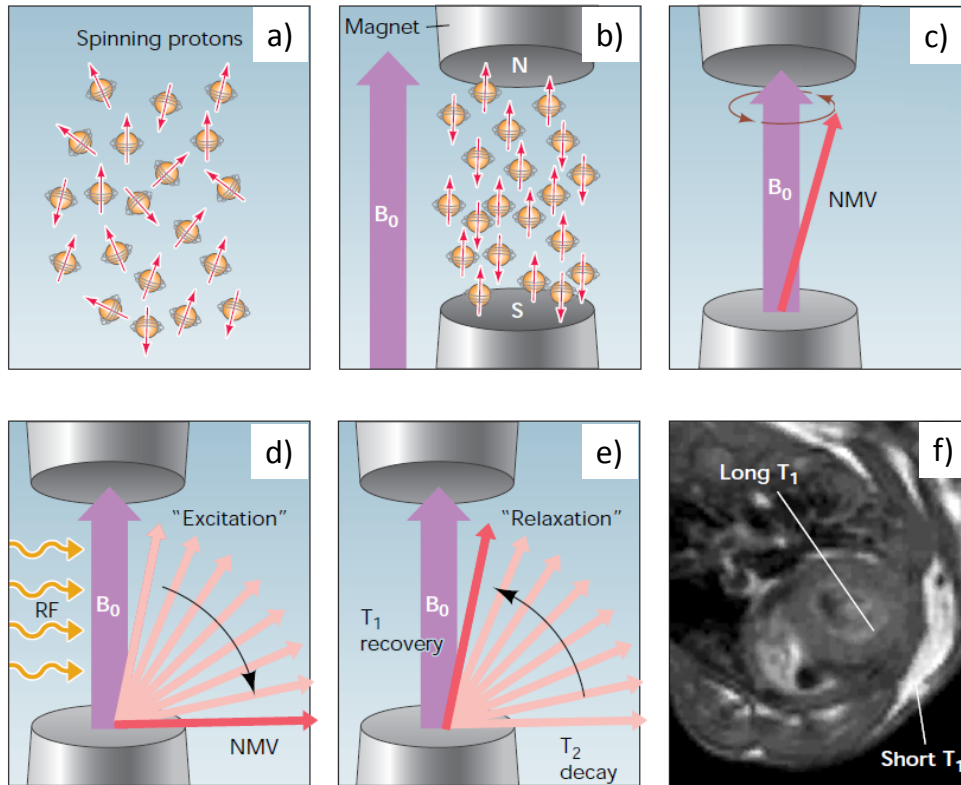


Figure 2.2. Basic description of magnetic resonance imaging (MRI): (a) to (e). A T_1 weighted image is shown in (f).¹²

Most of the MRI imaging in clinics focuses on the proton (hydrogen atom) due to its natural abundance in the human body. When a proton is placed in an external magnetic field (B_0), it will stop its random spin and align to the B_0 direction or longitudinal plane (Figure 2.1). The spins combine with B_0 and generate a net magnetization vector that precesses around B_0 at a frequency ω . The precessional frequency ω is represented by the Larmor equation:

$$\omega = \gamma \cdot B_0 \quad (2.1)$$

Here, γ is a constant known as the gyromagnetic ratio. If an RF pulse is applied to this precessing net magnetization, the protons will adsorb energy and change direction.

Application of an RF pulse is called excitation. The drop from the high energy level to lower energy level is called MR relaxation, and the collective effect of this drop in energy creates the T_1 and T_2 effects (Figure 2.1e).¹² Once the RF pulse is applied, a 180° flip is achieved, which is opposite of the magnetic field B_0 . The total magnetization is the sum of all proton magnetizations, and the magnetizations in the x-y plane are canceled out by the proton movement. After the RF pulse stops, the protons begin to recover back to the z direction, and eventually flip back to the 0° position, thus releasing all their energy. This is called T_1 (longitudinal) relaxation. If a 90° RF pulse is applied, the protons may synchronize and point at the x-y plane, while the z direction is canceled out. As time goes on, some of the protons spin faster and scatter from the original direction and at the end, the protons are spread out all over the x-y plane. This is called T_2 (transverse) relaxation. In a T_1 -weighted MRI image, tissues with a shorter T_1 will have a higher signal intensity than tissues with a longer T_1 (Figure 2.1f). T_1 -weighted contrast agents such as Gd^{3+} or Mn^{2+} shorten the T_1 of water in tissue, resulting in an increase in signal intensity in the tissues where the contrast agent has accumulated.

Contrast in MR images is based on the exchange of magnetization between the contrast agent and water protons. Contrast agents are broadly classified as negative and positive agents depending on whether they lead to signal loss or enhancement. Superparamagnetic iron-oxide nanoparticles (SPIONs) are a class of negative contrast (image darkening) agents for MRI. However, the negative contrast property of SPION has limitations in detecting tumors. For example, the tumor mass and the surrounding air passages embedded in tissue may both give dark signals in MR images, making it

difficult to differentiate the tumor. Also, SPIONs can be toxic if the Fe^{3+} from these accumulate in cells of the liver, brain, spleen, and lung.¹³ Another class of MRI contrast agents are positive contrast (image brightening) agents, such as gadolinium (Gd). The Gd^{3+} ion is a strong paramagnetic ion that shortens the T_1 and T_2 relaxation times of nearby water protons, and thereby provides an increased signal on the MR image.^{2-4,14} However, free Gd^{3+} ions can lead to nephrotoxicity and nephrogenic systemic fibrosis (NSF) in patients with renal diseases. To solve this problem, Gd^{3+} ions are conjugated with chelating compounds such as diethylenetriamine-pentaacetic acid (DTPA),^{15,16} and the resulting conjugates are chemically inert and safe.¹⁷ The standard clinical injection dose of Gd-chelates is about 0.1-0.3 mmol/kg, which leads to an average concentration of 0.5 mM in the extracellular space.^{16,18}

2.4. Vesicles and Liposomes

Vesicles are self-assembled containers formed in water by lipids, surfactants, or block copolymers.^{19,20} The molecules that form vesicles are amphiphilic, with a hydrophilic head and hydrophobic tail(s). The shell of the vesicle is a bilayer (ca. 2-5 nm in thickness) of these amphiphilic molecules, with the hydrophilic heads on both sides of the bilayer and thereby exposed to water, while the hydrophobic tails inside the bilayer are shielded from water. A vesicle can be considered to form by the folding of amphiphilic bilayers. Vesicles with only a single bilayer (or lamella) are called unilamellar vesicles (ULVs), while vesicles with several concentric bilayers are called multilamellar vesicles (MLVs) or “onions”.

The folding of bilayers into vesicles tends to occur only when the bilayers are present at low concentration; at high concentrations, bilayers form a lamellar phase.²⁷ The tendency for bilayers to fold is driven by a desire to minimize contact of the hydrophobes with water at the bilayer ends. Nevertheless, it is useful to remember that, at equilibrium, the amphiphiles usually exist as a lamellar phase; so, the vesicle state is often of limited stability. In other words, given sufficient time, vesicles will get disrupted and form a dilute lamellar phase. An important exception to this rule exists in the case of mixed surfactants, where vesicles can exist as equilibrium structures.²¹

Vesicles formed from lipids are referred to as “liposomes”. The term lipid usually refers to amphiphiles that have a biological origin and typically, such molecules have two hydrophobic (acyl) tails. Lipid bilayers constitute the membranes found at the boundary of every living cell as well as many intracellular organelles. The classification of lipids is done based on their headgroup type: for example, phospholipids have a phosphate moiety in their headgroup. Among the phospholipids, the phosphatidylcholines or lecithins are a common variety.

The tendency of lipids to form bilayers or vesicles can be rationalized from the geometry of these molecules. Generally speaking, the role of molecular geometry in dictating the self-assembly of amphiphiles can be understood by a term called the critical packing parameter or CPP, which is defined as follows:²²

$$\text{CPP} = \frac{a_{\text{tail}}}{a_{\text{hg}}} \quad (2.2)$$

where a_{hg} is the effective area of the amphiphile headgroup and a_{tail} is the average area of

the amphiphilic tail. Amphiphilic molecules having $\alpha_{\text{tail}} \approx \alpha_{\text{hg}}$, i.e., $\text{CPP} = 1$, tend to assemble into bilayers or vesicles (Figure 2.2). Note that the shape of these molecules resembles that of a cylinder. In contrast, molecules with a larger headgroup area than tail tend to favor curved structures, specifically micelles. A CPP of $\frac{1}{3}$ corresponds to spherical micelles while a CPP of $\frac{1}{2}$ corresponds to cylindrical micelles.

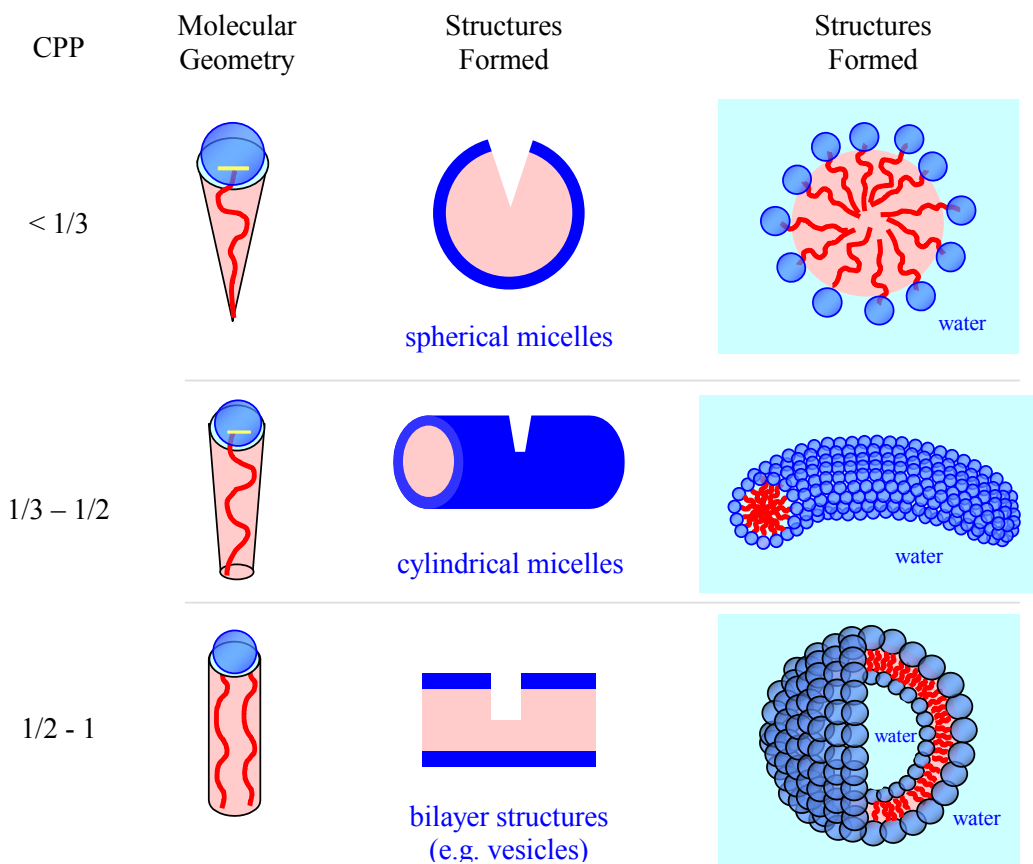


Figure 2.3. Schematics depicting the connection between the geometry of amphiphilic molecules and the structures they form in water. The hydrophilic heads of the amphiphiles are shown in blue and the hydrophobic tails in red.

2.5. Dynamic Light Scattering (DLS)

DLS probes the Brownian motion of particles in a fluid. This method can give a reliable estimate of particle size under certain limiting conditions. In a DLS experiment, the fluctuating intensity of light scattered from the sample is recorded at a certain angle θ . The fluctuations are then correlated to yield $g^{(2)}(q, \tau)$, the intensity autocorrelation function, vs. the correlation time τ :²³

$$g^{(2)}(q, \tau) = \frac{\langle I(q, t)I(q, t + \tau) \rangle}{\langle I(q, t)^2 \rangle} \quad (2.3)$$

Here q is the scattering or wave vector, and is defined as:

$$q = \frac{4\pi n}{\lambda} \sin\left(\frac{\theta}{2}\right) \quad (2.4)$$

where n is the refractive index of the medium. The relevance of q in DLS is that structural relaxations are probed over length scales on the order of q^{-1} .

The measured intensity autocorrelation function $g^{(2)}(q, \tau)$ can be converted into an electric field autocorrelation function $g^{(1)}(q, \tau)$ through the Siegert relation:

$$g^{(2)}(q, \tau) = 1 + f |g^{(1)}(q, \tau)|^2 \quad (2.5)$$

Here, f is an adjustable parameter called the coherence factor that depends on the instrument geometry. For a dilute solution of monodisperse spherical particles, the electric-field autocorrelation function is a single exponential whose time decay is determined by the translational diffusion coefficient of the particle D :

$$g^{(1)}(q, \tau) = \exp(-Dq^2\tau) \quad (2.6)$$

From the measured diffusion coefficient, the particle size can be obtained by the Stokes-Einstein equation:

$$D = \frac{k_B T}{6\pi\eta R_h} \quad (2.7)$$

where k_B is the Boltzmann constant, T the absolute temperature and η the viscosity of the solvent (assumed to be a Newtonian liquid). The size obtained from DLS is the *hydrodynamic radius* R_h . The hydrodynamic size is the bare particle size along with any solvation layer.

Chapter 3

Liposomes as Theranostic Nanoprobes

The results presented in this chapter have been published in the following journal article: Y. Kuo, C. Hung, R. Gullapalli, S. Xu, J. Zhuo, S. R. Raghavan and W. D. D'Souza, "Liposomal nanoprobes that combine anti-EGFR antibodies and MRI contrast agents: Synthesis and *in vitro* characterization." *RSC Advances*, 4, 33756-33764 (2014)

3.1. Introduction

The cells of many cancer tumors are known to over-express receptors for growth factors on their cell membranes.²⁴⁻²⁸ An example is the epidermal growth factor receptor (EGFR). An abundance of EGFR activates signaling pathways that ultimately leads to increased tumor proliferation, migration, and angiogenesis;²⁹ in turn, these cells also carry higher risk of metastasis.^{6,9,30,31} Targeted therapy for some cancers taking advantage of the molecular signature of over-expressed EGFR has emerged as a therapeutic option in recent years. Simple incubation of anti-EGFR monoclonal antibodies with carcinoma cell lines has been shown to inhibit tumor growth and invasion, presumably by blocking intracellular EGFR signaling pathways.^{7,32} This finding has been translated to the clinic: specifically, the FDA-approved EGFR-targeting monoclonal antibody *Cetuximab* (Bristol-Myers Squibb, Eli Lilly & Co.) is now used directly as a therapeutic agent against head-and-neck and colorectal cancers.^{9,33} Clinical trials have shown that *Cetuximab* in combination with radiotherapy improved the 5-year overall survival rate of

squamous cell carcinoma head and neck (SCCHN) patients to 46%, compared with 36% for the radiotherapy-only group.⁹ When combined with chemotherapy, *Cetuximab* lengthened the median overall survival time from 7.4 to 10.1 months.¹⁰

While the protocols for treating cancers with *Cetuximab* are well-established, clinicians currently cannot directly assess the *in vivo* effectiveness of such targeted agents over the course of a multi-week treatment regimen. Computed tomography (CT), positron emission tomography (PET), and magnetic resonance imaging (MRI) are the most useful live imaging technologies for cancer evaluation.¹ Among these methods, MRI is advantageous in that it provides high-resolution details and better contrast for discriminating between normal and tumor tissue, especially when used in conjunction with contrast agents. Contrast agents for MRI fall into two categories: negative-contrast (image-darkening) agents like iron oxide and positive-contrast (image-brightening) agents, such as gadolinium (Gd). The negative-contrast agents have limitations in detecting tumors since the airways surrounding tumors may yield dark signals as well, making it difficult to differentiate tumor from air in images. In comparison, positive-contrast agents like Gd are preferred. Gd^{3+} is a strong paramagnetic ion that shortens the T_1 and T_2 relaxation times of nearby water protons, thereby providing an increased signal on the MR image.^{2-4,14} While free Gd^{3+} ions are quite toxic,^{34,35} their toxicity can be sufficiently lowered by complexing Gd^{3+} ions with chelating compounds such as diethylenetriamine-pentaacetic acid (DTPA).^{15-17,36-38} The standard clinical injection dose of Gd-chelates is about 0.1–0.3 mmol/kg, which results in an average concentration of 0.5 mM in the extracellular space.^{16,18}

To observe EGFR-overexpressing cancer cells via MRI following targeted therapy, we have focused on constructing a nanoscale probe bearing both anti-EGFR antibodies and a positive MRI contrast agent, i.e., chelated Gd. Such a probe would be able to home in on tumor cells due to the antibodies, while the Gd would allow the corresponding area to be seen clearly on the MR image. For such a probe to be useful *in vivo*, it would have to be nontoxic and of overall size ~ 100 to 200 nm, which is optimal for *in vivo* circulation and concentration within tumors. Moreover, we wanted to develop a probe-synthesis method with as few steps as possible and using commercially available ingredients. The rationale was that a simple method would be scalable and allow synthesis of the probe in sufficient quantities to be eventually used in the clinic. These constraints led us to select liposomes as the optimal choice of nanoscale vehicle. Liposomes formed from phospholipids are much less toxic compared to other alternatives such as cationic dendrimers.³⁹ Moreover, they can be formed in a single step via self-assembly, which is a much simpler process than that required typically for polymer-based nanoparticles.

We report in this paper the engineering of liposomes that are non-covalently conjugated with both Gd-DTPA as well as *Cetuximab*, the therapeutic anti-EGFR antibody. The synthesis strategy is presented in Figure 3.1 and discussed further below. The resulting multifunctional liposomes are studied *in vitro* and shown to exhibit preferential binding to EGFR-rich SCCHN cells compared to low-EGFR-expressing cells. Moreover, we demonstrate the ability to track these structures using MRI.

Overall, these liposomes are a promising class of structures for tracking EGFR-overexpressing cancer cells in real time by MRI.

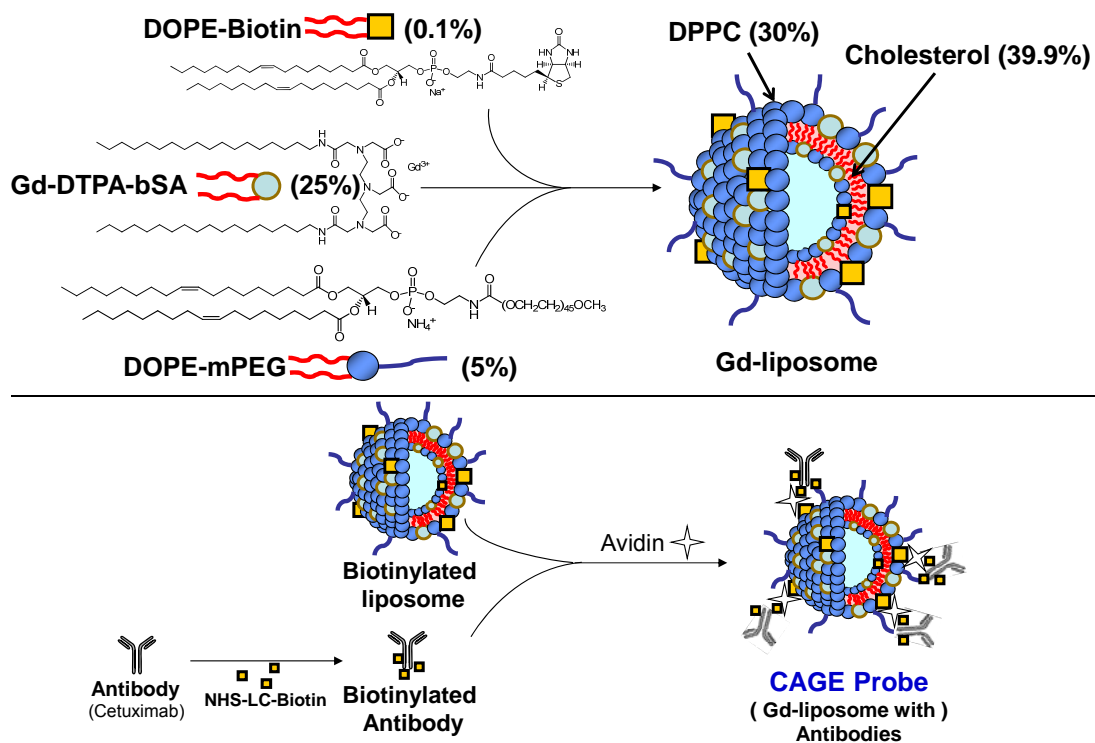


Figure 3.1. Structure of **CAGE** probes with **Chelated Gd** and antibodies to **EGFR** within a single structure of size ~ 100 nm. (Top) The lipids DPPC, Cholesterol, Gd-DTPA-bSA, DOPE-mPEG, and DOPE-biotin are combined to produce Gd-liposomes. (Bottom) The Gd-liposomes are combined with biotinylated *Cetuximab* (anti-EGFR antibody) and the tetrafunctional protein, avidin. The antibodies get attached to the Gd-liposomes via biotin-avidin interactions to form the CAGE probe. “CAGE” includes **chelated Gd** and antibodies to **EGFR**.

3.2. Experimental Section

Materials. 1,2-dipalmitoyl-sn-glycero-3-phosphocholine (DPPC); 1,2-dioleoyl-sn-glycero-3-phospho- ethanolamine-N-(biotinyl) (sodium salt) (DOPE-Biotin); DTPA-bis(stearylamide) (gadolinium salt) (Gd-DTPA-bSA); and 1,2-dioleoyl-sn-glycero-3-phosphoethanolamine-N-[methoxy(polyethyleneglycol) -2000] (DOPE-mPEG) were

purchased from Avanti Polar Lipids Inc. 1,1'-dioctadecyl-3,3,3',3'-tetramethyl-indocarbocyanine perchlorate (DiI) was purchased from Molecular Probes. Cholesterol, chloroform, and methanol was obtained from Sigma-Aldrich (St. Louis, MO). Premixed WST-1 cell proliferation reagent was purchased from Clontech. Sulfosuccinimidyl-6-[biotinamido]-6-hexanamido hexanoate (Sulfo-NHS-LC-LC-Biotin) and the corresponding biotin quantification kit were obtained from Thermo Fisher Scientific Inc.

Gd-Liposome Preparation. For Gd-liposome preparation, a lipid mixture consisting of DPPC, Cholesterol, Gd-DTPA-bSA, DOPE-mPEG, and DOPE-Biotin (molar ratio 30:39.9:25:5:0.1) was dissolved in a chloroform:methanol (4:1 v/v) mixture.⁴⁰ Fluorescent liposomes were created by including 2 μ M DiI. A dried film was formed by evaporating the solvent with a dry nitrogen stream, followed by vacuum desiccation for 24 h. The dried lipid film was rehydrated with water in 8 mM concentration and stirred at 60 °C for 2 h. The mixture was then ultrasonicated at 47.5 W for 15 min using a probe sonicator (Qsonica, Newtown, CT) to give unilamellar liposomes. pH was adjusted to 7.4 using PBS and samples were maintained at 4 °C before the experiments.

CAGE Probe Synthesis. 8 mL of 2 mg/mL *Cetuximab* (anti-EGFR antibody from Bristol-Myers Squibb) was purified using Sephadex G-25 column chromatography (GE Healthcare). Purified protein was analyzed by measuring OD at 280 nm using a NanoDrop 1000 (Thermo Fisher Scientific Inc.). To conjugate cetuximab with biotin,

the sulfo-NHS-LC-LC-Biotin was mixed with the purified *Cetuximab* and agitated at 4 °C for 24 h and purified via Sephadex G-25 column chromatography. The biotin quantification kit was used for measuring the biotin per *Cetuximab*. Finally, the biotinylated *Cetuximab* was combined with Gd-liposomes (at a 1:4 ratio of biotins on the antibody compared to the liposomes), and the tetrameric protein, avidin (from Sigma-Aldrich) was added at a molar ratio of 1:50 for avidin:total biotin.

Size Measurement. Vesicle size was measured by Dynamic Light Scattering (DLS) (Photocor Instruments). A 5 mW laser light source at 633 nm was used to analyze the size of vesicles. Studies were done at 25 °C with the scattering angle being 90°. All measurements were conducted in triplicate.

Zeta Potential. Surface potentials of vesicles were measured by a Laser Doppler Velocimetry technique (Malvern Zetasizer Nano ZS90) at a 90° scattering angle. Samples were placed in disposable polystyrene cuvettes (Folded Capillary Cell-DTS1060, Malvern). All measurements were conducted in triplicate.

Transmission Electron Microscopy (TEM). Samples were characterized by TEM on a Jeol JEM 2100 microscope at a 80-kV accelerating voltage. Carbon/formvar coated copper grids (Ted Pella, Inc.) were dipped into the solution containing the vesicle samples and then placed in a fume hood for 5 min. The dried TEM grids were then stained with a drop of 1% uranyl acetate (from Sigma-Aldrich) solution and the resulting grids were air-dried before taking images.

MR Properties of the Liposomes. For T_1 -weighted MR imaging, the samples (Gd-liposome/CAGE probe) were transferred to a 2 mL Eppendorff tube. Inversion recovery pulse sequence was used for the measurement of T_1 relaxation time by the least-squares algorithm using a 3.0 Tesla Siemens MAGNETOM-Trio system at 25 °C with the following settings: echo time (TE) = 12 ms, repetition time (TR) = 6000 ms. Thirteen different inversion-recovery waiting delay values (TI) between 40 ms and 2800 ms were measured (slice thickness = 5 mm). The signal intensity of each tube in the MRI was measured by placing a region of interest in the center of the cross-sectional images of the tube under different TI. T_1 values of each tube were calculated by fitting the collected data to the following function: $f(x) = m(1 - 2\exp(-TI/T_1))$ using Matlab, where $f(x)$ is the corresponding signal intensity and the fitting parameters are m and T_1 . A plot of $1/T_1$ versus Gd^{3+} concentration yielded a straight line with the slope being the samples' T_1 relaxivity value r_1 .

Cell Lines. SCCHN 15B cells were provided by Dr. Jennifer Grandis (University of Pittsburgh) and HEK293 human embryonic kidney cells were purchased from American Type Culture Collection. Cells were cultured in DMEM medium for HEK293 (Invitrogen) or RPMI-1640 medium for 15B with 10% FBS (Hyclone), 1% L-glutamine (Sigma-Aldrich) and maintained at 37 °C and 5% CO₂. Cells were propagated to 80% confluency prior to the *in vitro* assay. Phosphate buffered saline (PBS) was purchased from Invitrogen.

Flow-Cytometry Analysis of EGFR Expression. HEK and 15B were incubated at 37 °C for 1 h with Alexa Fluor labeled anti-EGFR antibody, sc-120 AF488 (green fluorescence, purchased from Santa Cruz Biotechnology, CA) at dilutions of 1/1000 and 1/3000 with PBS. Excess antibody was removed from the cells by washing three times with PBS and 5×10^5 cells were collected in 500 μ l PBS. EGFR expression for each cell line were analyzed by counting cells emitting green fluorescence by a FACScan (Becton-Dickinson). Additionally, Alexa Fluor signals in the cells were directly visualized by fluorescence microscope (Olympus BX60).

Cell Viability. Cells were plated in 96-well plates at a density of 10^4 cells per well containing 100 μ L of culture medium; after 24 h of cultivation, the cells were incubated with varying concentrations of vesicles. After 24 h of incubation, cell viability was evaluated by MTT assay using Premix WST-1 cell proliferation reagent (Clontech), and measuring the absorbance at 440 nm by a SpectraMax M2 spectrometer (Molecular Devices). All experiments were performed in triplicate.

Cell Targeting and Competition Assays. 10^4 cells were seeded onto an 8-well chamber slide. After overnight culture, cells were blocked with a culture medium containing 1% BSA at 37 °C for 30 min, and the CAGE probe or Gd-liposome was added at 2 mg/mL for 2 h of incubation at 37 °C. After washing with PBS three times, the samples were fixed with 2% paraformaldehyde, and slides were mounted with antifade, 4',6'-diamidino-2-phenylindole (DAPI)-containing fluorescent mounting media (EMD Chemicals), and visualized under a fluorescence microscope. For the

competition assay, 15B cells were incubated with 1:50 sc-120 AF488 antiEGFR antibody at 37 °C for 40 min, washed with PBS, and then incubated with different concentrations of CAGE probe for 1 h in a 37 °C incubator. After the same fixation steps above, slides were prepared and stored at 4 °C. The fluorescence intensity evaluation was done by ImageJ software (NIH). After manually selecting the region containing cells, total fluorescence intensity was acquired. To get the average fluorescence intensity per cell, the total intensity was divided by the number of cells. The result is the specific fluorescence intensity, which represents the average intensity of each cell.

Liposome Targeting Assay by MRI. 15B cells were cultured in several T175 flasks. In one flask, 12 mL of CAGE probe in cell medium (corresponding to 6 mM Gd³⁺) was added. In another flask, 12 mL of Gd-liposomes in cell medium (also corresponding to 6 mM Gd³⁺) along with free Cetuximab (equal to that in the flask with the CAGE probe) was added. Each flask was incubated for 1 h at 37 °C. The same process was repeated with additional cell-bearing flasks. Thereafter, all the cells were collected by centrifugation and washed three times with PBS. The cells were then fixed with 4% paraformaldehyde for 20 min at 4 °C. Then, the cells were placed in Eppendorff tubes for MR screening. The MR protocol is the same as described above to evaluate the Gd concentration bound to cells.

3.3. Results and Discussion

Preparation of Multifunctional Liposomal Nanoprobes

The base liposomal formulation employed here is a mixture of the phospholipid DPPC and cholesterol. We sought to conjugate both Gd-DTPA and antibodies to such liposomes. Towards this end, three additional lipids were introduced into the formulation, as shown in Figure 3.1. The first lipid, Gd-DTPA-bSA, has Gd-DTPA bound to two stearyl tails by amide linkages. The second lipid, DOPE-biotin, has two oleyl tails and a biotin attached to the lipid headgroup. A third lipid, DOPE-PEG was also added to the formulation; this lipid has two oleyl tails and a polyethylene glycol (PEG) oligomer (2000 Da) attached to the headgroup. The five molecules, i.e., DPPC, cholesterol, Gd-DTPA-bSA, DOPE-PEG, and DOPE-biotin were combined at a molar ratio of 30:39.9:25:5:0.1 for a typical formulation, with the overall lipid concentration being 6 mg/mL or 8 mM. Liposomes were prepared by sonication and we refer to the overall structures as Gd-liposomes. Note that the DOPE-PEG provides PEG chains on the exterior of the liposome, which impart steric stability and are expected to enhance the *in vivo* circulation time.⁴¹

The size and stability of Gd-liposomes were evaluated using dynamic light scattering (DLS). Liposome diameters for the typical composition noted above were measured to be 100 nm, 120 nm, respectively (Figure 3.2) and the sizes remained unchanged over three weeks of observation. The proportion of the Gd-DTPA-bSA lipid had an impact on liposomal stability. Since a higher fraction of Gd-DTPA-bSA in the liposomal bilayer would yield an increased signal in MRI, we attempted to increase this fraction (while reducing the cholesterol fraction). However, if the Gd-DTPA-bSA fraction was raised above 25 mol%, the liposomal diameter increased

substantially over time (data not shown), and in some cases, precipitation was observed. These observations indicate aggregation or destabilization of the liposomes. For these reasons, we fixed the Gd-DTPA-bSA fraction at 25 mol%.

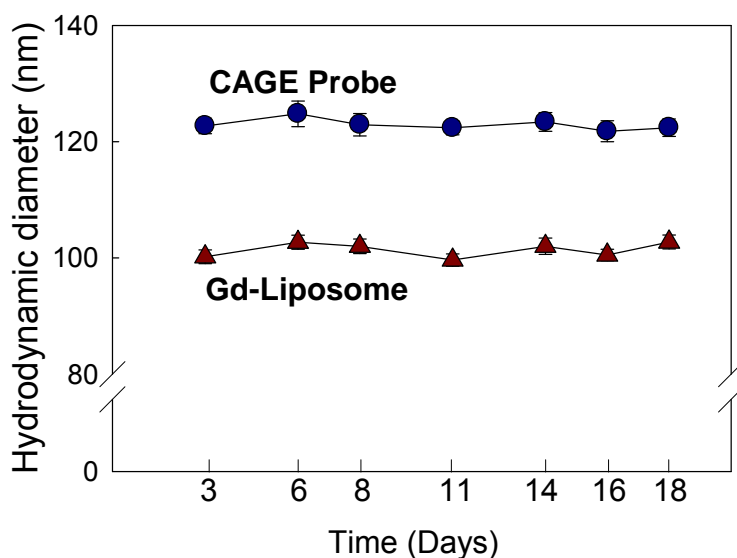


Figure 3.2. Liposome size and stability over a period of 18 days. Data are shown for Gd-liposomes (no antibody) and for the CAGE probes (liposomes with antibody attached). The sizes correspond to the hydrodynamic diameters from DLS.

The above Gd-liposomes had a zeta potential of +5.13 mV in water, indicating a net cationic nature. Among the lipids used, DPPC is zwitterionic and cholesterol is nonionic. The PE headgroups in DOPE-PEG and DOPE-biotin are anionic, but the fractions of these lipids in the formulation is low (5 and 0.1 mol%, respectively). Thus, the cationic nature of the overall liposomes is evidently arising from the Gd-DTPA-bSA lipid, and more specifically from the Gd^{3+} . The weak positive charge on the liposomes may be beneficial as it can provide electrostatic repulsions between them, which helps to stabilize the liposomes. The Gd-liposomes were also studied in PBS buffer and were again found to be stable over time. However, measurements of

the zeta potential in buffer did not yield consistent values, possibly because of the screening of electrostatic interactions by the ions in PBS. Thus, stability in PBS may be attributed primarily to steric repulsions from the PEG side chains. TEM images of Gd-liposomes negatively stained by uranyl acetate (Figures 3.3a, 3.3b) show that these liposomes are unilamellar spheres with diameters around 100 nm, which is broadly consistent with the DLS data above.

We then proceeded to attach antibodies to the Gd-liposomes. The antibody chosen was *Cetuximab*, the therapeutic anti-EGFR antibody, and we first chemically affixed biotins to it by the reaction shown in Figure 3.1. Each *Cetuximab* acquired ~3 biotins by this reaction. The biotinylated *Cetuximab* was then combined with the Gd-liposomes (bearing DOPE-biotin) in the presence of avidin, a tetrameric biotin-binding protein. A molar ratio of overall biotin:avidin = 50:1 was used and the ratio of biotins on Gd-liposomes versus biotins on *Cetuximab* was kept at 1:4. The components were mixed by agitation for 40 min and then maintained at 4 °C. In the process, *Cetuximab* becomes bound to the liposomes, as shown in Figure 3.1. We use the term “CAGE” to refer to the final liposomal structures since they combine chelated Gd as well as antibodies to EGFR. The CAGE probes were characterized by DLS (Figure 3.2) and TEM (Figure 3.3c, 3.3d). Figure 3.2 shows that the CAGE probes were also around 100 nm in diameter. They were slightly larger than the Gd-liposomes. This finding is consistent with antibody conjugation. TEM also reveals that the CAGE probes are unilamellar liposomes with sizes consistent with those measured by DLS.

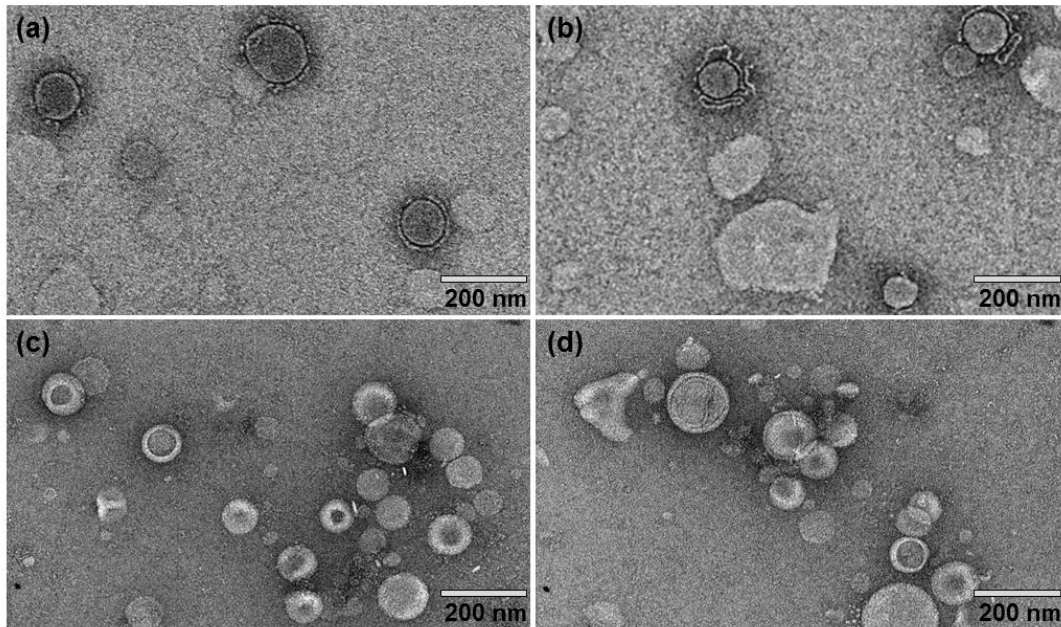


Figure 3.3. TEM images of liposome structures stained with 1% uranyl acetate. (a,b) Gd-liposomes; (c,d) CAGE probes.

Quantification of MR Contrast

Next, we quantified the MR signal of the above structures using a 3 T scanner. These studies were done with the Gd-liposomes and the CAGE probe. Gd-DTPA solutions were used as the standard for comparison. The longitudinal relaxation times T_1 for Gd-liposomes, the CAGE probe and Gd-DTPA solutions were measured at various dilutions. Plots of $1/T_1$ versus $[Gd^{3+}]$ for all sets of samples follow straight lines (Figure 3.4). The inverse relationship confirms that the higher the $[Gd^{3+}]$, the shorter the relaxation time T_1 . The slopes of the lines are defined as the relaxivities r_1 for each class of samples. r_1 was $3.3 \text{ mM}^{-1}\text{s}^{-1}$ for Gd-DTPA solutions, $8.07 \text{ mM}^{-1}\text{s}^{-1}$ for the Gd-liposomes and $3.93 \text{ mM}^{-1}\text{s}^{-1}$ for the CAGE probe. The r_1 values of Gd-liposomes and CAGE probes were 2.4 and 1.19 times higher than that of Gd-DTPA, respectively. This implies that the Gd-bearing nanostructures give rise to greater MR

contrast than Gd-DTPA. The r_1 enhancement for the Gd-liposomes may be the result of their being embedded in bilayers,⁴² which restricts the internal (rotational) motion of Gd. Higher relaxivity due to restricted internal motion of Gd has been reported previously.^{43,44} The CAGE probe may have decreased r_1 compared with Gd-liposomes because the linkage of avidin and the biotinylated antibody may shield the Gd in the liposomal bilayer from interactions with water, which would decrease the density of Gd-coordinated water molecules. It is worth noting that the T_1 time for water is 2383 ms and it is 2252 ms for the bare liposomes without Gd (negligible difference). In comparison, the inclusion of the Gd-DTPA-bSA lipid in the liposomes at a concentration of 2.0 mM reduces the T_1 time to 61 ms. This difference between bare and Gd-liposomes (2252 ms to 61 ms) is large enough to give appreciable contrast in MR images.

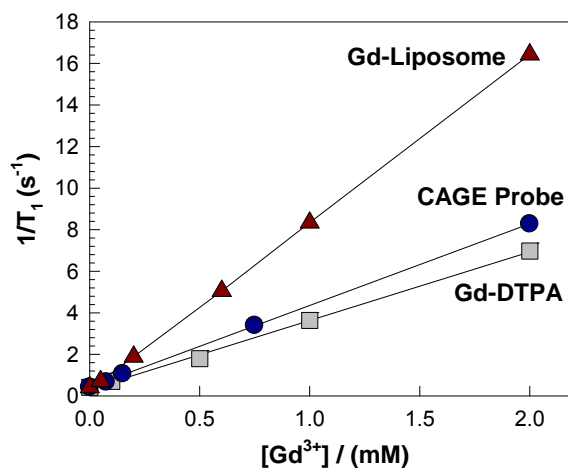


Figure 3.4. Relaxivity plots of $1/T_1$ vs. Gd^{3+} from MR measurements. Plots are shown for solutions of Gd-DTPA as well as for solutions containing Gd-liposomes. The slopes of the lines give the relaxivities for each sample (Gd-liposomes: $r_1 = 8.07 \text{ mM}^{-1}\text{s}^{-1}$, CAGE Probe: $r_1 = 3.93 \text{ mM}^{-1}\text{s}^{-1}$ and Gd-DTPA: $r_1 = 3.3 \text{ mM}^{-1}\text{s}^{-1}$).

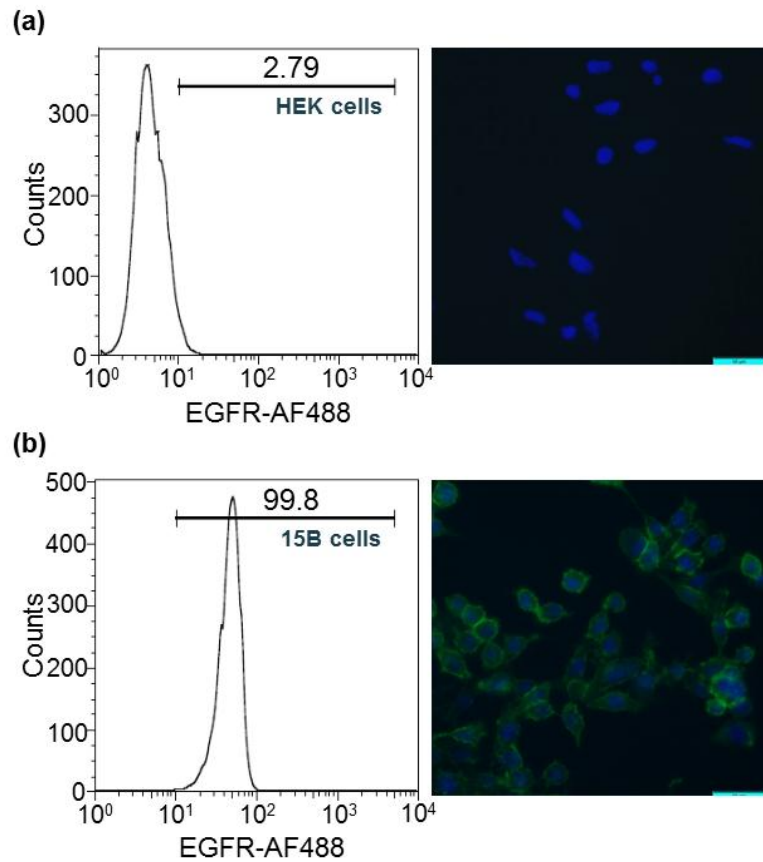


Figure 3.5. EGFR expression of normal HEK cells compared with that of SCCHN 15B cells by flow cytometry and fluorescence microscopy. (a) Very low Alexa Fluor fluorescence signal (green) is observed with HEK cells (2.79%) which implies low levels of EGFR expression. (b) In comparison, a high Alexa Fluor signal is found for 15B cells (99.8%). Note that in the micrographs, the cell nucleus stained by DAPI gives blue fluorescence, while the Alexa Fluor-bound antibody gives green fluorescence.

EGFR Expression: SCCHN vs. Normal Cells

As noted in the Introduction, most SCCHN cell lines are known to over-express EGFR, and one such cell line is the 15B line.^{45,46} We used SCCHN 15B as the positive control in targeting assays with our CAGE probes. For comparison, a human embryonic kidney cell line (HEK 293) was used to represent normal cells with low

EGFR expression. To confirm that SCCHN 15B cells exhibited higher EGFR expression levels compared to HEK 293 cells, each type of cells was contacted with an anti-EGFR antibody (sc-120 AF488) conjugated with the green fluorescent moiety, Alexa Fluor. Thereafter Alexa Fluor-positive cells were analyzed by flow cytometry and fluorescence microscopy. As expected,^{47,48} HEK 293 cells exhibited very low levels of EGFR expression with only 2.8% Alexa Fluor-positive cells detected by flow cytometry and almost no Alexa Fluor signal (green) in the fluorescence micrograph (Figure 3.5a). On the other hand, SCCHN 15B cells exhibited high expression levels of EGFR with nearly 100% of cells detected as Alexa Fluor-positive in flow cytometry (Figure 3.5b). These results confirmed the distinctive expression levels of EGFR between 15B and HEK 293 cells.

Cytotoxicity of CAGE probe on SCCHN 15B Cells

Before proceeding to the targeting assay, the cytotoxicity of the Gd-liposomes and the CAGE probes was investigated. SCCHN 15B cells were incubated with different concentrations of Gd-liposomes or CAGE probes for 24 h and the fraction of surviving viable cells was determined by the MTT assay. The data are presented in Figure 3.6. In the case of Gd-liposomes, more than 80% of cells remained viable at liposome concentrations between 0.01 to 1 mg/mL, while 50% of cells survived at 5 mg/mL. The assay thereby validates that the Gd-liposomes as relatively nontoxic, and this finding has also been confirmed by other researchers for similar liposomes.^{49,50} Compared with Gd-liposomes, the CAGE probes showed some toxicity to cells: 70%

of cells remained viable at a probe concentration of 1 mg/mL while 20% of cells survived at a concentration of 3 mg/mL.

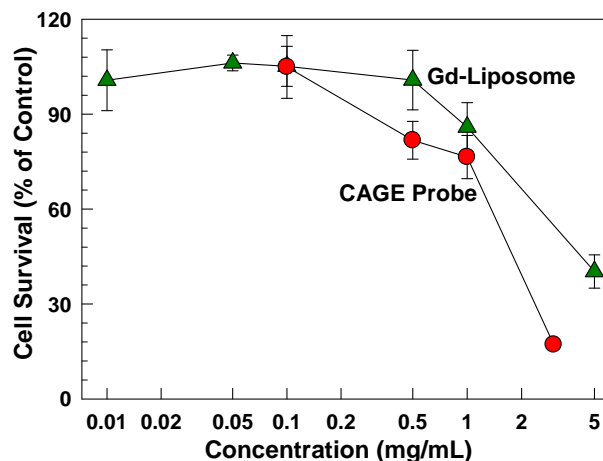


Figure 3.6. Cell viability (MTT) assay of 15B cells incubated with different structures. Gd-liposomes show low toxicity to cells, while the CAGE probes are somewhat toxic above 2 mg/mL.

Targeting Ability of CAGE Probes

To evaluate the targeting ability of CAGE probes, we chose a concentration of 2 mg/mL. The procedure for the experiment was based on that used by Mulder et al.⁵¹ and was designed to test whether the CAGE probes could specifically target EGFR-over-expressing cells. Gd-liposomes (no conjugated antibody) were used as the control. To assess targeting by fluorescence microscopy, an additional fluorescent lipid probe (DiI) was added to the liposomal bilayers of both the CAGE and the Gd-liposomes. We used live HEK 293 and SCCHN 15B cells for the targeting experiments. The experiments involved incubating the cells with the probes (or the controls) for 2 h, followed by washing to remove unbound probes, and then imaging of the cells for fluorescence from DiI. Although the probes were somewhat toxic at

this concentration over the 24 h time period in the MTT assay (Figure 3.6), they are not expected to significantly affect the cells over the shorter incubation time of 2 h in the targeting experiments.

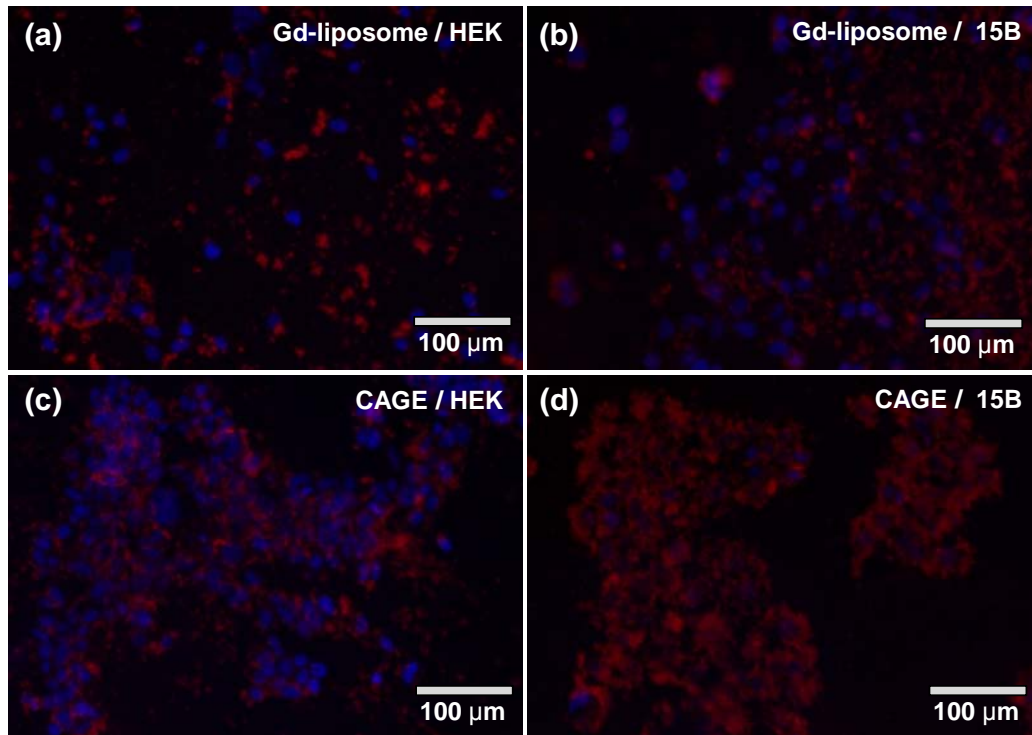


Figure 3.7. EGFR-mediated binding of Gd-liposomes and CAGE probes by HEK and 15B cells. Since the Gd-liposomes do not have any targeting function, they show some non-specific binding to both HEK cells (a) and 15B cells (b). On the other hand, the CAGE probes are able to bind significantly more to EGFR-overexpressing 15B cells (d) compared to HEK cells (c).

The results of the targeting experiments are shown by the fluorescence micrographs in Figure 3.7. The red color in the images indicates fluorescence from DiI in the liposomal membranes. As expected, the Gd-liposomes gave a similar weak red signal for both the SCCHN and normal cell lines, indicating that these liposomes randomly bind to cells without specificity (Figures 3.7a and 3.7b). On the other hand,

in the case of the CAGE probes, a significantly higher signal was observed with the EGFR-over-expressing SCCHN 15B cells compared to the normal HEK 293 cells (Figures 3.7c and 3.7d). These results indicate cell specificity and membrane binding of the CAGE probe against the 15B cells. The differences in fluorescence signals were quantified using Image J software. For the CAGE probes combined with 15B cells, the specific fluorescence intensity (per cell) was 41 ± 7 . In comparison, for the CAGE probes with HEK 293 cells, the intensity (per cell) was 12 ± 6 . Lastly, for the Gd-liposomes together with 15B cells, the intensity (per cell) was 14 ± 6 . Thus, there is a 3-fold higher fluorescence per cell in the case of the CAGE probe incubated with 15B cells, relative to the two controls. This higher signal is evidently a result of binding of the CAGE probe to EGFR receptors on the 15B cells.

Competitive Targeting of CAGE vs. anti-EGFR Antibody

To further evaluate the targeting ability of CAGE probes, we conducted a competition assay using the CAGEs against the anti-EGFR antibody (sc-120 AF488) (used also for EGFR quantification by flow cytometry). First, SCCHN 15B cells were incubated with the sc-120 antibody, which resulted in a strong green signal due to Alexa Fluor (green fluorescence) around the cells (Figure 3.8a). The same cells were contacted with a low concentration (0.1 mg/mL) of CAGE for 1 h, whereupon, the Alexa Fluor signal decreased and a dim red signal due to DiI in the CAGE was barely visible (Figure 3.8b). When the CAGE probes were added at medium concentration (0.8 mg/mL), the Alexa Fluor signal decreased further and a clear red signal from the CAGE became visible (Figure 3.8c). Finally, when a high concentration of CAGE (2

mg/mL) was introduced, the Alexa Fluor signal was nearly eliminated and all cells showed a distinctive red envelope, showing the binding of CAGE probes (Figure 3.8d). These results clearly show that the affinity of CAGE probes for EGFR on 15B cell membranes is comparable to that of the sc-120 antibody.

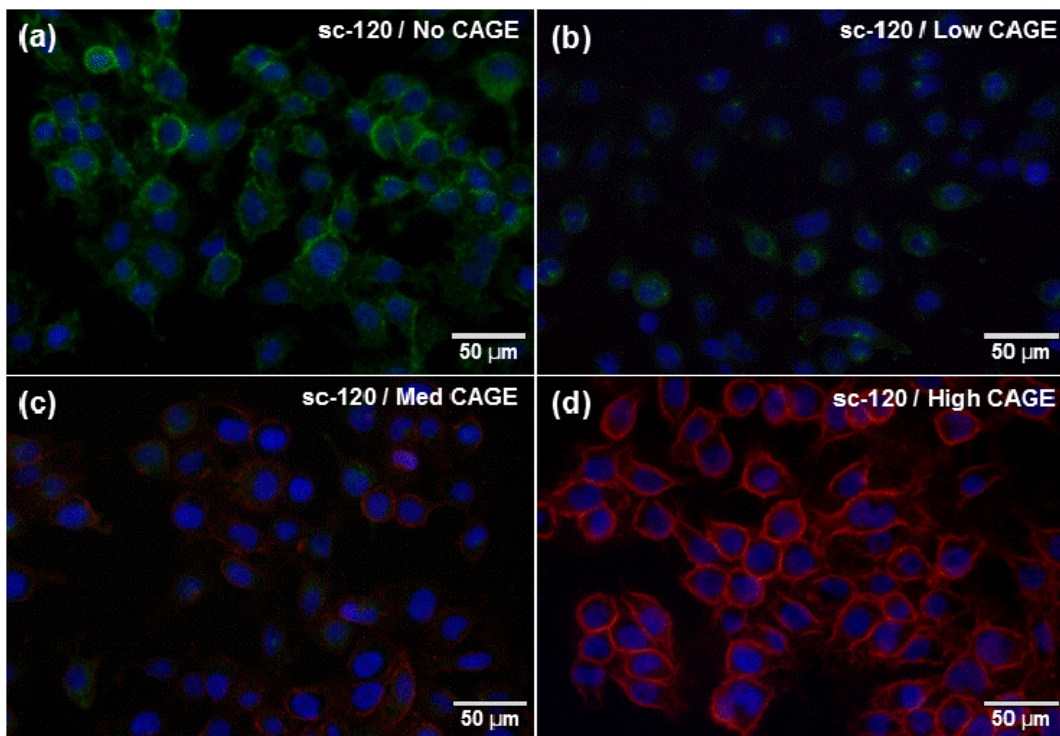


Figure 3.8. Competition assay of CAGE probes (red) with the sc-120 AF488 EGFR antibody (green) for evaluation of specific binding affinity in 15B cells. (a) 1:50 sc-120 alone (b) 1:50 sc-120, 0.1 mg/mL of CAGE, (c) 1:50 sc-120, 0.8 mg/mL of CAGE, (d) 1:50 sc-120, 2 mg/mL of CAGE.

In Vitro Study of CAGE-Targeted 15B Cells using MRI

Finally, we used MRI to screen a sample of 15B cells with bound CAGE probes. For this experiment, 15B cells were combined with CAGE probes at a concentration of 5 mg/mL (0.5 mM Gd) and incubated for 1 h. The cells were then washed with buffer to remove unbound CAGE, fixed and placed in an Eppendorf tube

for MRI scanning. For comparison, we also scanned tubes containing water and a 0.5 mM solution of Gd-DTPA. The corresponding cross-sectional images are shown in Figure 3.9; these images correspond to an inversion time, $TI = 1000$ ms. From images corresponding to various inversion times, the T_1 relaxation times were calculated. The water sample has a T_1 of 2252 ms, consistent with the relatively dark image. The 0.5 mM Gd-DTPA solution, in comparison, has a much lower T_1 of 381.4 ms, which reflects the much brighter image. The conjugate of Gd-liposome (which serves as a control with 0.5 mM Gd) incubated with 15B cells, resulted in a T_1 of 516.2 ms, which is 1.5 times higher than the Gd-DTPA solution. Finally, the 15B cells with bound CAGE probe yielded a T_1 of 379.3 ms, which is similar to the T_1 of 0.5 mM Gd-DTPA. The level of contrast in this image is more than sufficient for imaging purposes. Thus, we conclude that our Gd-bearing CAGE probes are capable of providing MRI images with sufficient resolution if the probes can effectively bind to their targets. Future studies will examine these probes *in vivo* using animal models of SCCHN.





Sample	Water	0.5mM Gd-DTPA	15B bound Gd-Lipo	15B bound with CAGE
T_1 (ms)	2383	381.4	516.2	379.3
				

Figure 3.9. MRI screening of CAGE probe-targeted 15B cells. T_1 values and MR images at $TI = 1000$ ms for pure water, 0.5 mM Gd-DTPA, Gd-liposome and CAGE probe-targeted 15B cells. T_1 values were calculated based on the intensity inside the circle by adapting a curve fitting tool in Matlab.

3.4. Conclusions

In this study, we have developed CAGE probes as a class of biocompatible nanostructures capable of binding selectively to cells that have an over-abundance of EGFRs on their membranes. Simultaneously, the CAGE probes are decorated with Gd-DTPA-bearing lipids, which enables them to provide positive contrast in MR images to regions with high levels of probe binding. In preparing these probes, we have deliberately chosen a simple, two-step procedure that uses materials that are commercially available, biologically-derived, biocompatible and non-toxic. The procedure involves self-assembly of a mixture of five lipids: DPPC, cholesterol, a lipid with Gd-DTPA, a PEGylated lipid, and a biotinylated lipid to yield liposomes of ~ 100 nm diameter. Thereafter, in a second self-assembly step, the above liposomes are combined with biotinylated *cetuximab* (commercial anti-EGFR antibody) in the presence of the linker protein avidin. The resulting CAGE probes are stable in solution and show minimal toxicity to cells. Using fluorescence-based *in vitro* assays, we have confirmed that the probes bind preferentially to EGFR⁺ cells compared to EGFR⁻ cells. The MR relaxivity of these probes is sufficient to provide reasonable levels of positive contrast in MR images. In future studies, we will examine the binding of CAGE probes *in vivo* using animal models of SCCHN. The eventual goal is to use these probes to track the uptake of targeted agents in patients during the course of a typical 7-week cancer treatment. It is hoped that the tracking ability using MRI will eventually enable physicians to personalize the treatment for each patient and thereby help to improve outcomes for these patients.

Chapter 4

Micro-Erythroosomes and Their Colloidal Properties

4.1. Introduction

In Chapter 3, we had investigated the use of liposomes as theranostic structures. As is well-known (see Chapter 2), the structure of liposomes mimics the structure of a typical biological cell, i.e., both liposomes and cells have a lipid membrane enclosing internal contents.^{52,53} Given this analogy, one can turn back to biological cells and ask if it is possible to empty the contents of the cells and thereby obtain the equivalent of liposomes. In this context, erythrocytes, i.e., red blood cells (RBCs), from animal or human sources are an attractive candidate. They are responsible for transporting oxygen from the lungs to the tissues and exchanging carbon dioxide from the tissues to the lungs for expiration. RBCs have a life span of 120 days in the human body, which greatly exceeds the lifetime of any synthetic drug carrier that has been developed so far.⁵⁴ Also, RBCs have no nucleus or organelles and also do not contain nucleic acid matter; they are essentially containers filled with hemoglobin and therefore are relatively easy to empty.

The idea of using erythrocytes as carriers for a substance other than (or in addition to) hemoglobin dates back to the 1970s.⁵⁵ Empty erythrocytes were created by osmotic shock, centrifugation, and repeated washing. These are termed “erythroosomes” or “ghosts”; here, we will refer to them as micro-erythroosomes (MERs) (to distinguish from the smaller nano-erythroosomes that we will discuss in Chapter 5. MERs tend to be about the same size as the original RBCs (i.e., around 4 μm in diameter). Several methods have

been reported to encapsulate drugs or other chemicals in MERs, such as electrical pulse methods,⁵⁶ hypo-osmotic methods,⁵⁷⁻⁵⁹ and hydrophobic insertion into the membrane.^{60,61} However, there is still only a limited number of studies on these structures, especially from the viewpoint of colloid science.

In this study, we have isolated MERs from bovine blood and explored their use in the targeted delivery of solutes. We have studied the ability of MERs to encapsulate solutes such as the MRI contrast agent Gd-DTPA in their core. We have also attempted to decorate the MER membranes with targeting agents such as anti-EGFR antibodies. Our studies show that MERs have several interesting properties that may make them suitable for delivery applications.

4.2. Experimental Section

Materials. Bovine blood was purchased from Lampire Biological Laboratories. 1,2-dioleoyl-sn-glycero-3-phospho- ethanolamine-N-(biotinyl) (sodium salt) (DOPE-Biotin) was purchased from Avanti Polar Lipids. Dextran-FITC were obtained from Sigma-Aldrich. 1,1'-dioctadecyl- 3,3,3',3'-tetramethyl-indocarbocyanine perchlorate (DiI) and 3,3'-Dioctadecyl-oxacarbo-cyanine perchlorate (DiO) were purchased from Molecular Probes. Phosphate buffered saline (PBS); Fetal bovine serum (FBS); Streptavidin magnetic beads; Avidin-FITC were purchased from Life Technologies.

Microerythrocytes Preparation. The microerythrocytes were prepared from whole blood by centrifugation as previously described in Chapter 4.⁶² Briefly, red blood cells (RBCs) were first separated from 100 mL whole blood by centrifugation (3 times at 2000 rpm, 10 min). RBCs were washed with cold PBS (pH 7.4). Then the RBCs was resuspended in hypotonic PBS (pH 7.4) which contained 0.14 M NaCl, 0.01 M phosphate, 0.003 M KCl and incubated for 5 min on ice. The solution was transferred to a Beckman SW28 ultracentrifuge and spun at 12,000 rpm for 10 min at 4°C. Subsequently, the pellet was resuspended in cold PBS to give the MERs. pH was kept at pH 7.4 using PBS and samples were maintained at 4°C before the experiments. Fluorescent MERs were created by including 2 µM DiI in ethanol, while biotinylated MERs were made by including DOPE-biotin. MERs with antibodies were created as follows: biotinylated Cetuximab (anti-EGFR antibody from Bristol-Myers Squibb) was combined with biotinylated MERs (at a 1:5 ratio of biotins on the antibody compared to the MERs), and the tetrameric protein, avidin (from Sigma-Aldrich) was added at a molar ratio of 1 : 60 for avidin : total biotin, followed by a PBS wash.

Size Measurement. MER sizes were extracted from optical microscope images via the ImageJ software (NIH). Sizes were averaged over 150 structures in an image. All calculations were conducted in triplicate.

Zeta Potential. Surface potentials of ERs were measured by a Laser Doppler Velocimetry technique (Malvern Zetasizer Nano ZS90) at a 90° scattering angle. Samples

were placed in disposable polystyrene cuvettes (Folded Capillary Cell-DTS1060, Malvern, UK). All measurements were conducted in triplicate.

Encapsulation in Microerythrocytes. MERs were prepared by the method above and incubated with FITC-Dextran in 0.1x PBS for 1 h at 4°C.⁵⁸ A sealed sample was then added to 10x PBS (isotonic conditions) and placed in a water bath at 37°C for various times. The samples were observed by the Zeiss LSM710 microscope and the fluorescence intensity was measured by the plate reader (Ex: 492 nm, Em: 518 nm).

Cell Targeting Assay of Microerythrocytes. 10^4 15B cells were seeded onto an 8-well chamber slide. After overnight culture, cells were blocked with a culture medium containing 1% BSA at 37°C for 30 min, and the MERs prepared as described above were added for 1 h of incubation at 37°C. After washing with PBS three times, the samples were fixed with 2% paraformaldehyde, and the slides were mounted with antifade, 4',6'-diamidino-2-phenylindole (DAPI)-containing fluorescent mounting media (EMD Chemicals), and visualized under a fluorescence microscope.

4.3. Results and Discussion

Preparation of Microerythroosomes (MERs)

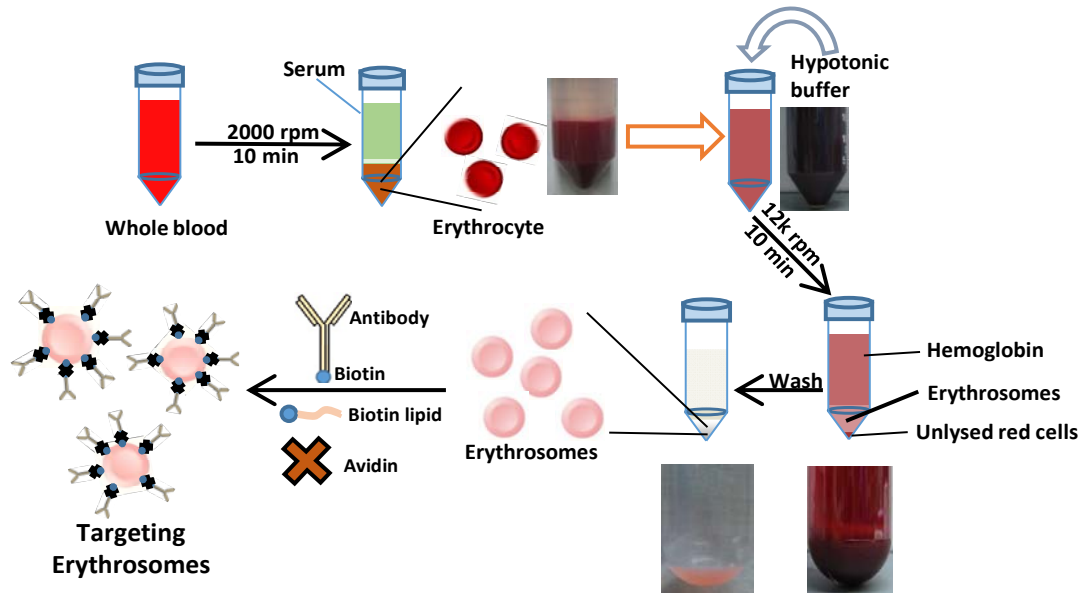


Figure 4.1. Preparation of MERs from bovine whole blood. Red cells were separated, burst via hypotonic PBS to cause hemoglobin release, and purified via ultracentrifugation to remove the hemoglobin in the supernatant. Unlysed MERs are in the bottom pellet. The MERs were then functionalized with antibody using biotin-avidin linkages.

The procedure for preparing MERs is shown in Figure 4.1. We use bovine blood, which has a hematocrit, i.e., volume fraction of RBCs, of about 20% (in human blood, the hematocrit is about 40%). In terms of number density, we measured the concentration (by a cytometer) of cells in the blood to be about 3×10^9 cells/mL. RBCs were separated from the white cells, platelets, and serum by centrifugation, i.e., by exploiting differences in density between the different components. The separated RBCs were then placed in hypotonic PBS. This induced the hemoglobin in the cells to be leached out due to the osmotic gradient between the cells and the solution. The process was carried out over a couple of cycles, and at the end, the pellet at the bottom of the centrifuge tube contains the cells without hemoglobin, which have a characteristic pink or white color. These are

the microerythrocytes (MERs), and they can be resuspended as a stable dispersion either in deionized (DI) water or in PBS. The concentration of MERs measured by the cytometer was 1 to 1.5×10^9 /mL, i.e., the yield was between 30 to 50%.

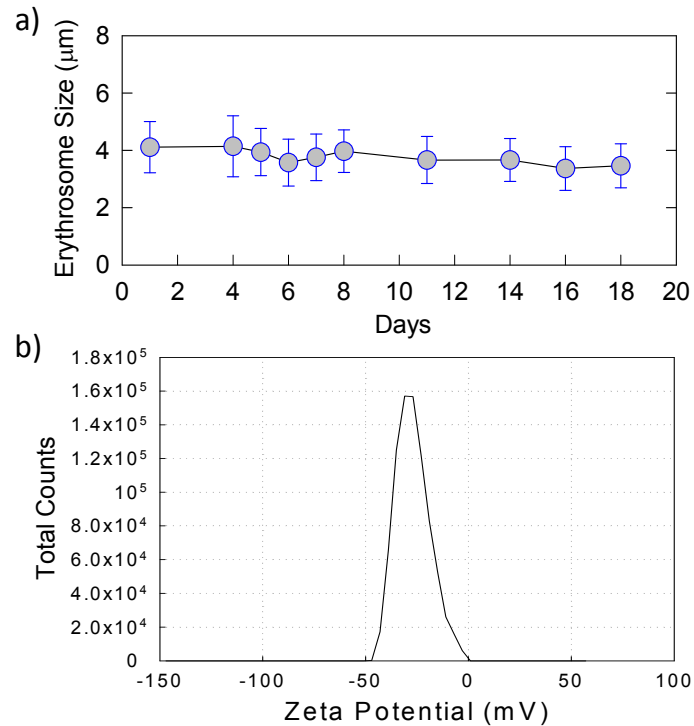


Figure 4.2. Stability of microerythrocytes. a) MERs in PBS over a period of two weeks. b) Zetapotential of MERs is about -30 ~ -40 mV.

Characteristics of MERs

The size and stability of MERs were evaluated using optical microscopy. The MERs in isotonic PBS ranged from 2 to 6 µm in diameter, and the mean was ~ 4 µm. The same size was maintained over 18 days of observation (Figure 4.2a). The shape of the MERs was similar to the original RBCs, i.e., both were biconcave discs in isotonic solution. However, in hypotonic solutions, their shape changes to an isotropic sphere. The surface charge of the MERs was measured, and their zeta potential was found to be

between -30 and -40 mV (Figure 4.2b). These measurements confirm that the MERs have a net negative charge, which helps in stabilizing these structures against aggregation. The negative charge is likely to come from anionic lipids such as phosphatidylserine (PS) in the MER membranes.⁶³ Overall, our results suggest that the MERs are identical to the RBCs in terms of their size, shape, and membrane properties, with the only difference being that the core of the MERs is empty whereas the RBCs contain hemoglobin.

Functionalization of MERs

The membranes of MERs can be tagged with other lipids quite easily. For example, the red fluorescent lipid DiI was incorporated into MERs as follows. A sample of DiI in ethanol was mixed with a suspension of MERs in PBS. The mixture was then centrifuged and the pellet was resuspended in water. When observed under fluorescence microscopy, we found a number of red spherical shell-like structures in this sample, indicating incorporation of DiI into the MER membranes. A similar procedure was repeated with the green fluorescent lipid DiO, thus forming MERs with green-fluorescent membranes. Next, we combined the DiI-coated MERs and the DiO-coated MERs into the same sample in a 1:1 ratio by weight. Figure 4.3 is a micrograph of this sample overlaying the green and red fluorescence. We note the co-existence of green and red-stained spherical shells in this figure. The structures are swollen because they are in water (hypotonic environment), which is why they appear as spheres rather than discs. Interestingly, there was no crossover of lipid from one membrane to another, i.e., the fluorescence of each population of MERs was retained over time. This shows that the MER membranes are intact. Note that the crossover of lipids across water from one

membrane to another is generally prohibitively slow due to the hydrophobicity of the lipids.

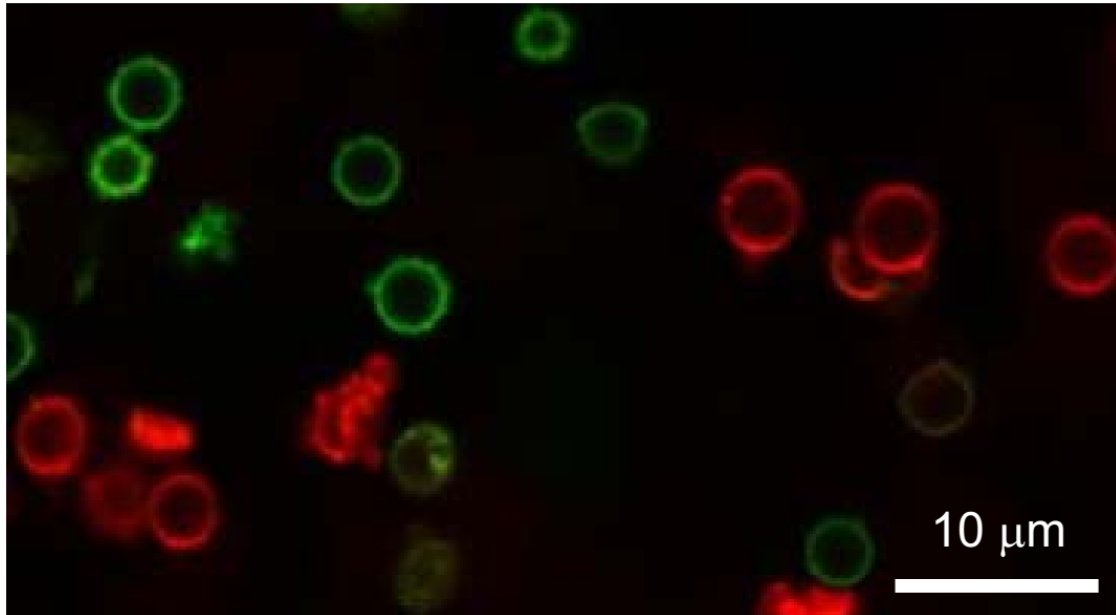


Figure 4.3. Decoration of MERs with fluorescent lipids. The figure is a superimposition of green and red fluorescence from a sample containing a 1:1 mixture of MERs with the red fluorescent lipid DiI and MERs with the green fluorescent lipid DiO. The structures are suspended in water (hypotonic solution), and hence are swollen into spheres.

Overall, the experiment above shows that MERs can be manipulated as colloidal entities, much like giant vesicles. In this regard, MERs are different from their parent RBCs. To show this, we mixed a sample of DiI in ethanol with a suspension of RBCs in PBS. This mixture was centrifuged and the pellet was resuspended in water or buffer. Examination by fluorescence microscopy showed that very few of the RBCs were stained red by the DiI; most of the RBCs showed no fluorescence at all. Thus, when the RBCs are intact, they do not readily permit foreign lipids to be incorporated into their membranes.

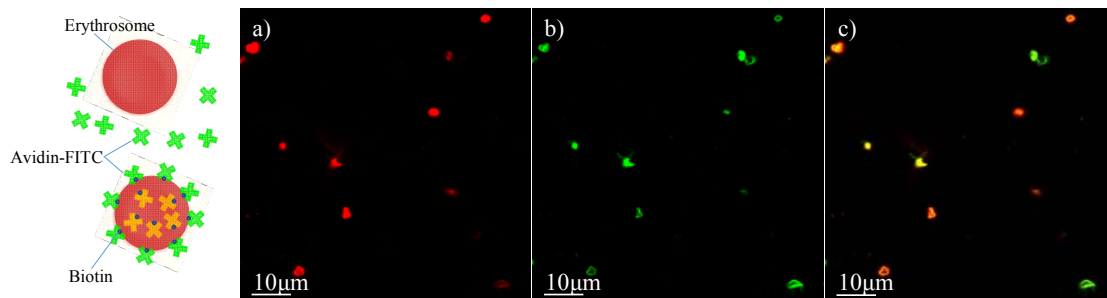


Figure 4.4. Surface modification of MERs by biotin-avidin interactions. (a) MERs with DiI and DOPE-Biotin show red fluorescence. (b) To this, when avidin-FITC is added, we see green fluorescence at the same spots, indicating binding of avidin to the biotins on the MERs. (c) A superimposed image of green and red fluorescence confirms this binding.

Next, we used biotin-avidin interactions to functionalize the MERs. First, we tagged the MERs with two lipids: DiI and DOPE-biotin and suspended these in PBS. The resulting structures should show red fluorescence due to the DiI. Then, we combined these MERs with the protein avidin, which itself has been tagged with the green fluorescent molecule FITC. The mixture was then subjected to washing steps to remove unbound avidin-FITC. When this sample is imaged by fluorescence microscopy, we see structures that simultaneously show red fluorescence due to the DiI (Figure 4.4a), as well as green fluorescence due to the FITC (Figure 4.4b). The combined image confirms that the two kinds of fluorescence overlap with each other. In turn, this indicates that the avidin-FITC binds to the biotins on the MER membranes by strong non-covalent interactions. Note that this route for MER surface modification is very straightforward because it involves self-assembly rather than chemical reactions. Traditional surface modification of nanoparticles is done using chemical reactions, i.e., the formation of covalent bonds such as between NHS and carboxyl groups, maleimide and thiol groups, or aldehyde and amine groups.^{2,62,64} Chemical routes are usually more difficult and

complex because the synthesis schemes do not always go to completion, and moreover, because purification of the modified structures can be quite tedious.

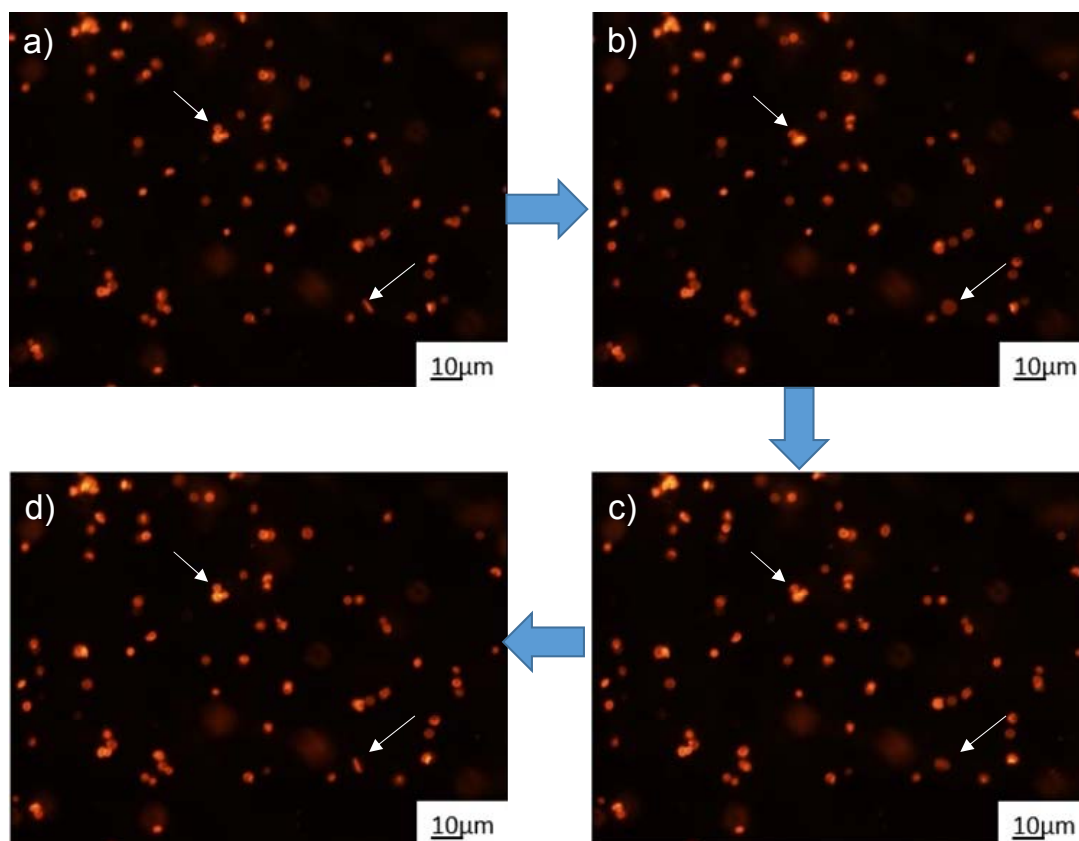


Figure 4.5. Imparting magnetic properties to MERs. This is done by binding streptavidin-coated magnetic beads to MERs with DiI and biotin. The images are stills from a movie, in order from a to d. The arrows indicate the motion of MERs at different time points.

Another use of biotin-avidin interactions is demonstrated in Figure 4.5. Here, we start with MERs decorated with DiI and DOPE-biotin and we incubate these with streptavidin-conjugated magnetic beads (1 μm in diameter). The mixture is then observed under a fluorescent microscope. The MERs show red fluorescence due to the DiI. The magnetic beads cannot be seen, but are bound to the MERs due to biotin-avidin

interactions. When an external magnet is rotated or swayed, the MERs move along with the magnet, as shown by Figure 4.5a-d, which are still images from a movie. Note that some MERs, which are clearly disc-like, change their orientation under the magnet, i.e., the disc is seen edgewise in Figure 4.5a whereas the disc is flat in Figure 4.5b. Overall, we are able to impart magnetic properties to the MERs by exploiting biotin-avidin interactions.

Solute Encapsulation and Release from MERs

Next, we evaluate the encapsulation capability of MERs within their aqueous cores. For this, dextran-FITC (molecular weight $\sim 4,000$ Da) was chosen as the solute. To encapsulate the solute in the MERs, we first added the solute to the MER suspension at room temperature under hypotonic conditions. During this time, the MER membrane gets ruptured and some of the solute gets internalized. We then altered the conditions so as to facilitate resealing of the membrane. This involves increasing the osmolarity of the solution to 1X PBS, warming to 37°C , and holding at that temperature for some period of time (typically 1 h). Following this “resealing procedure”, the sample is centrifuged and the pellet is resuspended in isotonic PBS.

The importance of the resealing procedure for solute encapsulation is shown by Figure 4.6. First, as a comparison, we show data for the RBCs, which still contain hemoglobin. In this case, we add the solute, follow the resealing procedure, and then resuspend the RBCs in PBS. A small extent of fluorescence is seen in Figure 4.6b, indicating that only a little of the dextran-FITC gets into the RBC core. Next, we consider

the MERs, with the solute encapsulated, but no resealing done. In this case, the unsealed MERs do not show any fluorescence at all (Figure 4.6d). Finally, the sealed MERs are shown in Figure 4.6f, and in this case, substantial fluorescence is seen, indicating that an appreciable amount of dextran-FITC is present in the cores of the MERs. Note that the RBCs show higher contrast in the bright field image than the MERs because of the hemoglobin in them. The sealed MERs are slightly smaller than the RBCs, but their fluorescence signal is much higher. The different fluorescence intensities from the above samples were also quantified using a plate reader. Relative to the unsealed MERs (= 1), the intensities for RBCs and sealed ERs were 6.5 and 26, respectively. These values are consistent with the microscopy results. They indicate that sealed ERs can accommodate 4 times as much payload than RBCs.

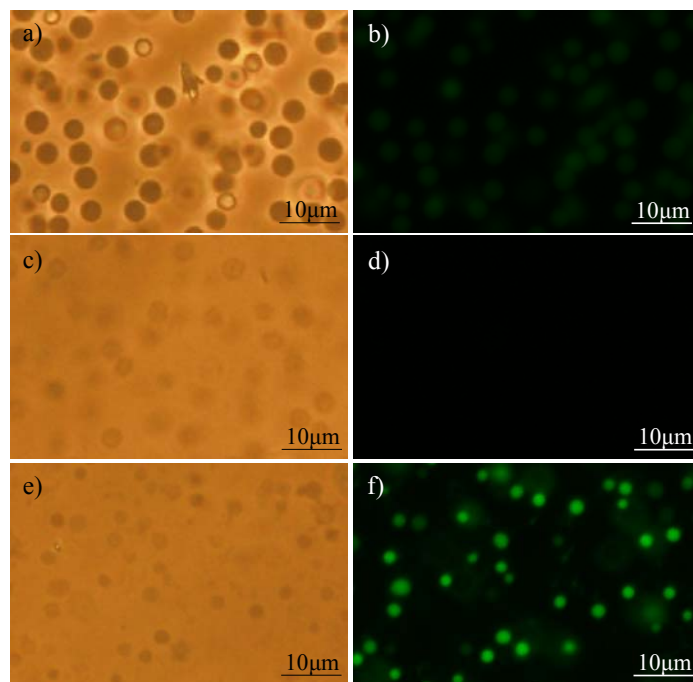


Figure 4.6. Encapsulation of dextran-FITC in various structures. The images on the left are bright field views while those on the right are for green fluorescence. (a) and (b) sealed RBCs; (c) and (d) unsealed ERs; (e) and (f) sealed ERs.

The above data indicate that MERs must be sealed for effective encapsulation of cargo. Since the sealing process is critical, we investigated the variables involved, including sealing time and sealing temperature. The control sealing conditions employed earlier were to hold the sample at 37°C for 1 h in 1X PBS. Results were compared in terms of the fluorescence intensity I from the plate reader, with I normalized to a value of 1 for a sealing time of 0 min. Our data show that longer sealing times give higher encapsulation. Sealing times of 5 min, 40 min, and 60 min gave $I = 7, 14$ and 16 , respectively. Thus, a minimum sealing time of 40 min is recommended. The sealing temperature was not found to be a significant factor. If the temperature was raised from 37°C to 65°C with the sealing time constant at 60 min, I dropped by about 40%. Also, some of the MERs in the latter case were found to be fragmented in the microscopic field of view (data not shown). This may be because high temperatures denature some of the proteins in the MER membrane.

We proceeded to study the encapsulation and release of a small molecule from the MERs. The molecule is Gd-DTPA, i.e., chelated gadolinium, which is a well-known MRI contrast agent. We encapsulated this in the MERs and then used MRI to evaluate the release profile. At $t = 0$, all the solute was in the MERs. As time progressed, some of the solute leaked out of the MER membranes into the external solution. The solute concentration in the external solution was measured, and the data are shown for the cumulative % released vs. time (Figure 4.7). Since sealing time can affect the loading of cargo, we obtained these release profiles for two different sealing times: 10 min and 60 min (sealing temperature of 37°C in both cases).

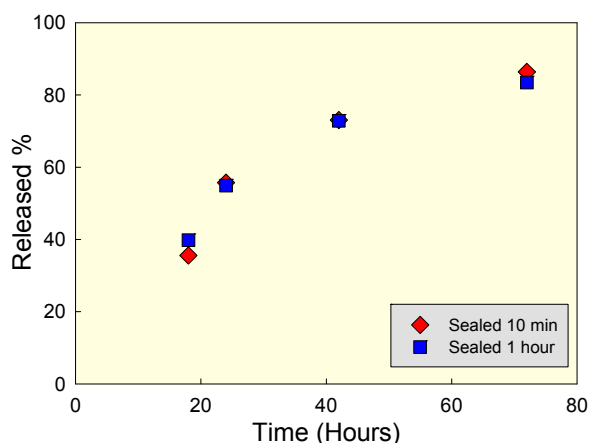


Figure 4.7. Release of Gd-DTPA from MERs. Data are shown for two different sealing times.

Figure 4.7 shows similar release profiles for the two sealing times. Note that 50% of the encapsulated Gd-DTPA is released over the first 24 h and more than 80% over 3 days. However, the amounts encapsulated under the two conditions were different. With 10 min of sealing time, 0.14 mM Gd-DTPA was encapsulated initially in the MERs. In comparison, with 60 min of sealing, 0.21 mM of Gd-DTPA payload was present in the MERs, which is 1.5 times higher than the 10 min sample. Thus, a longer sealing time allows more solute to be encapsulated, although the rate of solute release seems to be independent of the solute concentration.

Targeting MERs to Specific Cells

The ability to deliver cargo to specific targets is a critical challenge for drug delivery. To facilitate this, we attached antibodies to the MERs using the procedure shown in Figure 4.1. MERs with DiI and DOPE-biotin were linked to anti-EGFR-biotin by an avidin bridge. We then studied the binding of these MERs with anti-EGFR antibodies to 15B cells, which are a class of cells that overexpress EGFRs. Our controls

were the MERs alone and the MERs with biotin (both also had DiI for visualization by fluorescence microscopy). When the controls were combined with 15B cells, there was negligible non-specific binding, and the structures were removed easily during the washing steps. Thus, no fluorescence is seen in Figures 4.8a and 4.8b. For the MERs with anti-EGFR, on the other hand, there was tight binding to the cells, reflected in terms of significant red fluorescence in Figure 4.8c. Thus, we see that MERs can be functionalized to allow their targeted binding to specific cell types.

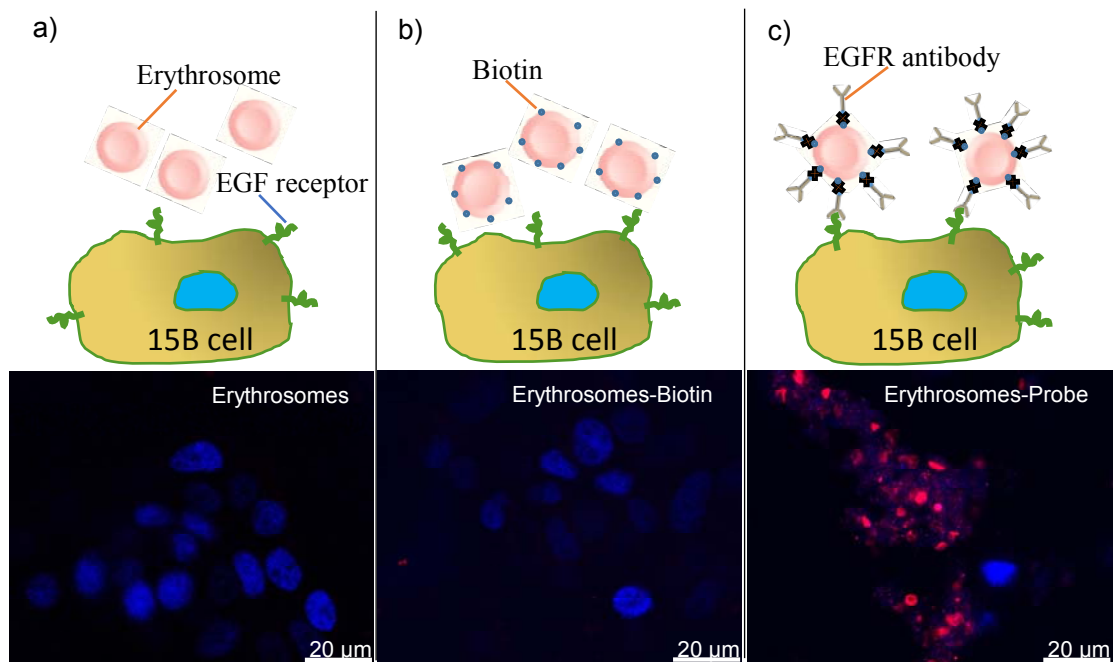


Figure 4.8. Targeted binding of MERs with 15B cells (which overexpress EGFRs). (a) MERs alone, (b) MERs with biotin, (c) MERs with anti-EGFR antibodies. The blue fluorescence represents the DAPI nucleus counterstain, and the red fluorescence comes from the DiI on the MERs.

4.4. Conclusions

In this study, we have developed microerythrocyte probes as a biocompatible and natural carrier that selectively binds to cells that have over-expressed EGFRs on their membranes. The MER probes derived from RBCs formed a robust system that kept the membrane intact with constant shape and structure, and was capable of targeting and releasing small molecular cargo *in vitro*. We have proved that the ethanol integration method can be a simple and useful way to achieve the cell surface modification, which only involved ethanol and target ligands, without complicated chemical reaction. Through the easy integration method, we decorated the MERs with dye, biotin, and even EGFR antibody, which can be further developed for various applications. As for the drug release function, the MERs reached 50% Gd-DTPA release about 24 hrs, and this implies the reduced dose of imaging application for MRI. The selective delivery combined with drug release turned the MER probes into an effective cancer theranostic agent. Not only just for the low cost and commercial availability of carrier MERs, but the eventual goal is to synthesize these probes from patients' own blood, which will help minimize immune response and personalize the specifically targeting therapy.

Chapter 5

Nano-Erythroosomes and Their Colloidal Properties

5.1. Introduction

In this Chapter, we study smaller (~ 100 nm) versions of the microerythroosomes (MERs), which we term nanoerythroosomes (NERs). The NERs are comparable in size to liposomes. As noted in Chapter 3, liposomes are a versatile class of colloidal vehicles for pharmaceutical and biomedical applications. They are typically prepared by a high-shear process, such as extrusion of a lipid/water mixture through a porous filter, or by sonication.⁶⁵⁻⁶⁷ Liposomes typically have nanoscale diameters (~ 100-200 nm) and a unilamellar bilayer membrane. They can be made to encapsulate solutes of interest such as drugs or proteins, and they can also be endowed with specific biochemical properties through moieties attached to the membrane.⁶⁸⁻⁷⁰

However, liposomes also suffer from some problems, especially that of limited colloidal stability, i.e., they tend to aggregate or phase-separate when stored at room temperature.⁷¹ The lack of stability arises because liposomes do not represent a thermodynamically stable phase; this is particularly evident from the fact that high-shear is needed to form these structures. Colloidal stability can be improved by attaching hydrophilic polymers to the liposomal surface – specifically, chains of polyethylene glycol (PEG).⁷² The presence of PEG chains sterically stabilizes the liposomes and thus improves their stability,⁷³⁻⁷⁵ however, optimal stability is obtained only for certain lengths and graft densities of PEGs on the liposomes. Thus, researchers who work with

liposomes still have to confront stability issues. For example, it is customary to either use liposomal samples right after preparation or to store these samples in a refrigerator at 4°C to improve the stability window. Liposomal stability is also frequently affected by the media of choice: for example, stability can be poor for liposomes in the presence of serum or cell-growth media.^{76,77} Finally, liposomes can also be destabilized when the sample goes through freeze-thaw cycles.⁷⁸

As noted in Chapter 4, the idea of creating erythroosomes (also called “ghosts”) from erythrocytes dates back to the 1970s.⁵⁵ Original erythroosomes were about the same size as the original erythrocytes (i.e., around 4 μm in diameter). More recently, in the 1990s, nanoscale analogs of these ghosts were reported by Al-Achi and Boroujerdi^{79,80} and by Lejeune et al.^{81,82}; the latter group coined the term “nanoerythroosome” (NER) for these structures. NERs were created by these authors by subjecting the microscale ghosts to a high-shear process, i.e., sonication or extrusion. The resulting structures had nanoscale dimensions (diameters ~ 100 to 200 nm) and are thus directly comparable to conventional liposomes.

Although NERs have been known for more than 20 years, they seem to have attracted limited interest from the scientific community. One reason is that their physical, i.e., colloidal properties, have not been systematically studied. For example, we have been unable to find any papers on NERs in traditional journals of colloid science or nanoscience; the few papers that have appeared have all been in pharmaceutical journals.^{72,81,83-89} In this paper, we report a systematic study of NERs from a colloidal

point of view. We use scattering and microscopic techniques to characterize these structures; in particular, the techniques of cryo-transmission electron microscopy (cryo-TEM) and small-angle neutron scattering (SANS) are used for the first time. We have also compared NERs with conventional liposomes prepared from lipids, especially from the viewpoint of colloidal stability and solute encapsulation. Our results confirm that NERs are unique structures with exceptional stability and that they have significant potential for controlled release and targeted drug delivery applications.

5.2. Experimental Section

Materials. Bovine blood was purchased from Lampire Biological Laboratories. 1,2-dipalmitoyl-sn-glycero-3-phosphocholine (DPPC); 1,2-dioleoyl-sn-glycero-3-phosphoethanolamine-N-(biotinyl) (sodium salt) (DOPE-Biotin) and 1,2-dioleoyl-sn-glycero-3-phosphoethanolamine-N-[methoxy(polyethyleneglycol)-2000] (DOPE-mPEG) were purchased from Avanti Polar Lipids Inc. Cholesterol and Dextran-FITC were obtained from Sigma-Aldrich. 1,1'-dioctadecyl-3,3,3',3'-tetramethyl-indocarbocyanine perchlorate (DiI) and 3,3'-Dioctadecyloxacarbocyanine perchlorate (DiO) were purchased from Molecular Probes. Phosphate buffer saline (PBS); Fetal bovine serum (FBS); Avidin-FITC were purchased from Life Technologies. Dialysis cassettes were purchased from Thermo Fisher Scientific Inc. The antibodies, mouse anti-EGFR (sc-120) and corresponding mouse IgG_{2a} (sc-3878) control, were purchased from Santa Cruz Biotechnology, CA. Microbial transglutaminase (mTG)⁹⁰ and Protein G⁹¹ were provided by Dr. William Bentley (University of Maryland).

Nanoerythroosome Preparation. The procedure for preparing NERs was described schematically in Figure 5.1. This procedure is adapted from that used in previous studies^{89,92} with some modifications. First, 100 mL of bovine whole blood was taken, and RBCs were separated from it by centrifuging three times (2,000 rpm, 10 min). Between each step, the RBCs at the bottom of the tube were washed and resuspended in PBS. After the third step, the RBCs were transferred to a hypotonic solution to remove the hemoglobin. The hypotonic solution was composed of PBS with 0.14 M NaCl, 10 mM Na-phosphate, and 3 mM KCl. The RBCs were incubated in the hypotonic PBS for 5 min on ice. This was then transferred to an ultracentrifuge (Beckman SW28) and run at 12,000 rpm for 10 min at 4°C. The pellet (cells with hemoglobin removed) was collected and resuspended in the hypotonic PBS, and this process was repeated thrice. Subsequently, the sediment was resuspended in cold PBS and ultracentrifuged at 20,000 rpm for 10 min at 4°C; this was again repeated thrice. The final pellet contains the washed MERs (Figure 5.1c). These MERs were placed in PBS (pH of 7.4) and this solution was ultrasonicated using a probe sonicator (Qsonica) at 47.5 W for 15 min to give the NERs.

Liposome Preparation. Two types of liposomes were prepared according to previous procedures.⁶⁷ Bare liposomes contained a mixture of DPPC:Cholesterol = 60:40 (molar ratio). PEGylated liposomes employed a mixture of DPPC: Cholesterol: DOPE-mPEG = 55:40:5 (molar ratio). The pertinent lipid mixture was dissolved in chloroform and a dried film was formed by evaporating the solvent with a dry nitrogen stream, followed by vacuum desiccation for 24 h. The lipid film was rehydrated with PBS and stirred at 60°C for 2 h. The mixture was then ultrasonicated at 47.5 W for 15 min using a probe sonicator

(Qsonica) to give liposomes. Samples were maintained at 4°C before experiments. The total lipid concentration in both the final samples was 6 mM.

Cell and Particle Count. The number densities of RBCs and MERs (microscale structures) were determined using a hemocytometer (Fisher Scientific). Trypan blue was used to provide contrast to the structures before the counts were taken.

Size Measurement. Sizes of nanostructures were measured by Dynamic Light Scattering (DLS) at 25°C using a Photocor-FC instrument. The instrument has a 5 mW laser light source at 633 nm, and the scattering angle was fixed at 90°. All measurements were done in triplicate.

Zeta Potential Measurements. Zeta potentials of the various nanostructures were measured by a Laser Doppler Velocimetry technique using a Malvern Zetasizer NanoZS90 at a 90° scattering angle. Samples were placed in disposable polystyrene cuvettes. All measurements were done in triplicate.

Cryo-Transmission Electron Microscopy (Cryo-TEM). C-Flat holey carbon grids with a hole size of 1.2 μm were purchased from Electron Microscopy Sciences. Grids bearing aqueous solutions of the nanostructures were plunged into liquid ethane (−183°C) using a Gatan CryoPlunge3, so as to form vitrified specimens. The samples were thereafter imaged on a JEOL-2100 LaB6 TEM at liquid nitrogen temperature.

Small-Angle Neutron Scattering (SANS). Measurements were made on the NG-7 (30 m) beamline at NIST in Gaithersburg, MD. Neutrons with a wavelength of 6 Å were selected. Three sample-detector distances were used to probe a range of scattering vectors from 0.004 to 0.4 Å⁻¹. Samples were studied in 2 mm quartz cells at 25° C. The scattering spectra were corrected and placed on an absolute scale using calibration standards provided by NIST. The data are shown for the radially averaged intensity I as a function of the scattering vector $q = (4\pi/\lambda)\sin(\theta/2)$, where λ is the neutron wavelength and θ is the scattering angle.

Stability Tests. To assess colloidal stability, the two liposome samples and the NERs were first studied in the presence of FBS. 1 mL of FBS was added to 2 mL of both liposomes and NERs samples under 4°C incubation. Sizes were measured periodically by DLS. Next, the same samples were subjected to freeze-thaw cycling. During each cycle, the samples were frozen at -20°C for 24 h and then thawed at room temperature for 2 h. Size changes were measured by DLS after every cycle. All measurements were conducted in triplicate.

Solute Encapsulation. To encapsulate the solute (dextran-FITC) in the NERs, the following procedure was used. The starting point was with the pellet of MERs, which was obtained as described above. This pellet was combined with 1 mg/mL of the solute in PBS, followed by sonication as above. This converts the MERs to NERs and the solute is internalized during this process. The next step was to “re-seal” the disrupted NER membranes to ensure that the solute remains inside. For this, the sample was subjected to

a freeze-anneal-thaw cycle. That is, the sample was cooled to 4°C, then immediately transferred to a water bath at 37°C and annealed at that temperature for 40 min, then cooled back to room temperature. At the end of this cycle, we have “sealed” NERs containing the solute, but there is also free solute in the outer solution. To remove free solute, the solution was purified using size-exclusion chromatography (SEC), i.e., by passing it through a 1 × 20 cm column packed with Sephadex G50 resin (from Sigma-Aldrich). The same dextran-FITC solute was also encapsulated in the PEGylated liposomes. In this case, 1 mg/mL of the solute was added to the solution used to rehydrate the lipid film. The mixture was sonicated as before and then purified by SEC using the same column as above.

Solute Release Studies. Release of the dextran-FITC solute from the liposomes and the NERs was measured as follows. First, 3 mL of the pertinent sample was injected into the dialysis cassette, which was then placed into a large flask containing 1 L of PBS buffer (see Figure 5.6). The buffer was replaced with fresh buffer every 1 h at the outset and thereafter every 4 h. 120 µL of sample was collected periodically from the dialysis bag and the fluorescence intensity of solute in the sample was measured by a SpectraMax M2 spectrometer (Molecular Devices) (Ex: 492 nm, Em: 518 nm). These were converted to concentrations using a standard curve. As the solute is released into the external buffer, the solute concentration in the bag keeps decreasing. These data were normalized into release curves, as shown in Figure 5.6.

Antibody Conjugation. To conjugate the antibody to NERs, the following procedure was used, as shown schematically in Figure 5.7. For this, stock solutions of recombinant glutamine-tagged protein G (50 $\mu\text{g}/\text{mL}$) and mTG enzyme (1 unit/mL) were obtained from the Bentley lab. First, protein G was covalently linked to the NERs using mTG (Figure 5.7). To accomplish this, final concentration of 2.5 $\mu\text{g}/\text{mL}$ of the protein G solution was combined with 1 mL of NERs, and then 4×10^{-3} unit/mL of the mTG solution was added. The mixture was subjected to mild shaking at room temperature for 30 min. Then the NERs with protein G were washed and purified with 100 kDa cutoff centrifugal filter tube (EMD Millipore) to remove free protein G. They were resuspended in PBS and then 10^{14} of antibody molecules were added. This mixture was incubated overnight at 4°C under mild shaking. Antibody-laden NERs were then purified by centrifugation as above. For visualization by fluorescence microscopy, the same NERs were also tagged with a fluorescent lipid dye called DiI. This was done during the NER formation process: 2 μM DiI was dissolved in ethanol, and 20 μL of this solution was added to 1 mL of the MERs, followed by sonication to yield NERs.

Cell Lines. SCCHN 15B cells were provided by Dr Jennifer Grandis (University of Pittsburgh). Cells were cultured in RPMI-1640 medium with 10% FBS and 1% L-glutamine (from Sigma-Aldrich). Cells were maintained at 37°C in 5% CO_2 .

Cell Targeting Studies. 10^4 15B cells were seeded onto an 8 well chamber slide at 37°C. Cells were propagated to 80% confluency (typically overnight). Then, RPMI medium containing 1% bovine serum albumin (BSA) was added to the cells for 30 min. The BSA

eliminates non-specific binding of the antibodies to the cells. Two NER samples were studied, one with the mouse IgG_{2a} control antibody and the other with the mouse anti-EGFR antibody. Both NERs were also tagged with DiI. 100 μ L of each sample was added to separate wells containing the 15B cells and left to incubate for 30 min. Thereafter, the cells were washed three times with PBS to remove unbound nanostructures. The samples were then fixed with 2% paraformaldehyde. Cells were then stained with 4',6'-diamidino-2-phenylindole (DAPI) (EMD Chemicals), which is a dye that binds to the nuclei in the cells. Then the cells were visualized under a fluorescence microscope.

5.3. Results and Discussion

Preparation of Nanoerythroosomes (NERs)

The procedure for preparing NERs is shown in Figure 5.1. We use bovine blood, which has a hematocrit, i.e., volume fraction of erythrocytes, of about 20% (in human blood, the hematocrit is about 40%). In terms of number density, we measured the concentration (using a cytometer) of erythrocytes in the blood used here to be about 3×10^9 cells/mL. Erythrocytes were separated from the white cells, platelets, and serum by centrifugation (Figure 5.1a), i.e., by exploiting differences in density between the different components. The separated erythrocytes were then placed in a hypotonic phosphate-buffered saline (PBS) solution. This induced the hemoglobin in the cells to be leached out due to the osmotic gradient between the cells and the solution (Figure 5.1b). The process was carried out over a couple of cycles, and at the end, the pellet at the bottom of the centrifuge tube contains the cells without hemoglobin, which have a characteristic pink or

white color (Figure 5.1c). These are the erythroosomes, having diameters around 3 to 4 μm , and they can be resuspended as a stable dispersion either in deionized (DI) water or in a buffer (PBS). The concentration of erythroosomes measured by the cytometer was $1 - 1.5 \times 10^9$ /mL, i.e., the yield was between 30 to 50%. To reduce their size to the nanoscale, we subjected the dispersion of erythroosomes to high shear using a tip sonicator for 15 min (Figure 5.1d). This resulted in a stable dispersion of empty NERs with sizes (see below) around 100 nm. The mass concentration of NERs in the final sample was estimated to be about 18 mg/mL, i.e., ~ 1.8 wt%.

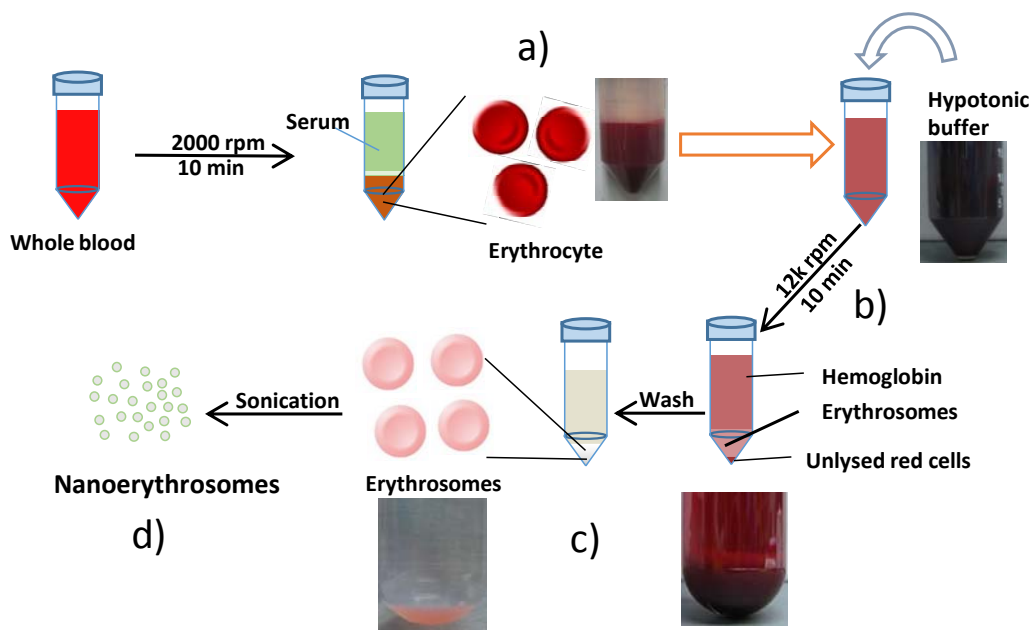


Figure 5.1. Preparation of ERs and NERs from bovine whole blood. Red cells were a) separated, burst via hypotonic PBS to cause hemoglobin release, and b) purified via ultracentrifugation to remove the hemoglobin in the supernatant. c) Unlysed ERs are in the bottom pellet. d) The NERs were prepared from transparent ERs via sonication.

Characterization of NERs

NER sizes were characterized using dynamic light scattering (DLS). DLS yields the hydrodynamic diameter (D_h) of particles assuming that the particles are discrete and non-interacting. Figure 5.2 plots the D_h of NERs in two media: DI water and PBS. In both cases, the NERs have a diameter ~ 105 – 110 nm and this size remains approximately constant over more than two weeks of observation. Thus, the NERs show excellent colloidal stability. The sizes of NERs are comparable to those of typical liposomes made by extrusion. We found no significant effect of sonication speed or time on NER size: for example, sonication times between 3 and 15 min gave identical NER sizes (data not

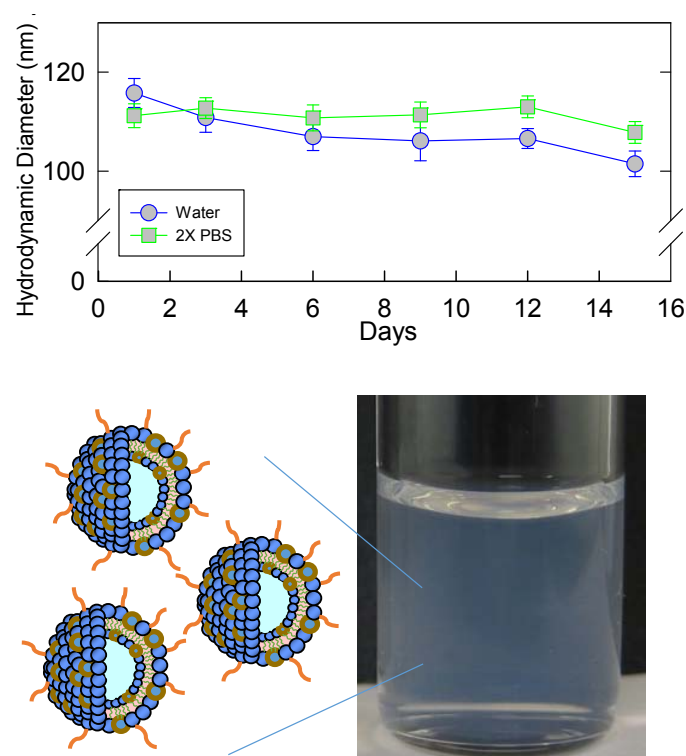


Figure 5.2. Sizes (hydrodynamic diameters from DLS) of NERs over a period of two weeks in water (circles) and in PBS (squares). NERs in PBS show a bluish tint.

shown). In comparison, liposomes typically become smaller if they are sonicated for longer times or at higher shear rates.

Next, the surface charge densities of NERs were measured using zeta potential measurements. The zeta potential was found to be around -30 to -40 mV, which indicates a fairly strong negative charge on these structures. The membranes of bovine NERs are expected to consist of phospholipids ($\sim 50\%$), cholesterol ($\sim 25\%$) and membrane proteins ($\sim 25\%$). The net negative charge may arise from anionic phospholipids as well as from anionic membrane proteins. The magnitude of this charge is probably high enough to ensure colloidal stability of the NERs via electrostatic repulsions alone. But in addition, NERs are also expected to be sterically stabilized by hydrophilic sugar side-chains, attached to either the lipids or the proteins on the external leaflet of the bilayer membrane.

The morphology of the NERs was then investigated by cryo-TEM. In this technique, the structure in an aqueous colloidal dispersion is preserved by rapid vitrification. Cryo-TEM has been extensively used on liposomes previously, but to our knowledge, not thus far on NERs. Figure 5.3a shows a typical cryo-TEM image of NERs suspended in DI water. Most of the structures appear in the image as circles with a thin, dark shell: these correspond to spherical, unilamellar vesicles. The spherical vesicles are by far the most common structure in this sample, but a few other morphologies are also seen. In Figure 5.3a, we see a few dark lines, which correspond to flat, disklike vesicles, observed edgewise. Also, the arrow indicates one instance of a biconcave disk with a unilamellar membrane; this is the shape usually associated with erythrocytes. Vesicles

that deviate from the unilamellar structure are also seen sometimes, including a concentric bilamellar vesicle (Figure 5.3b), and instances of two or three unilamellar vesicles inside a larger unilamellar vesicle (Figure 5.3c, 5.3d). For the most part, individual structures range in diameter from 90–120 nm, which is broadly consistent with the size measured by DLS.

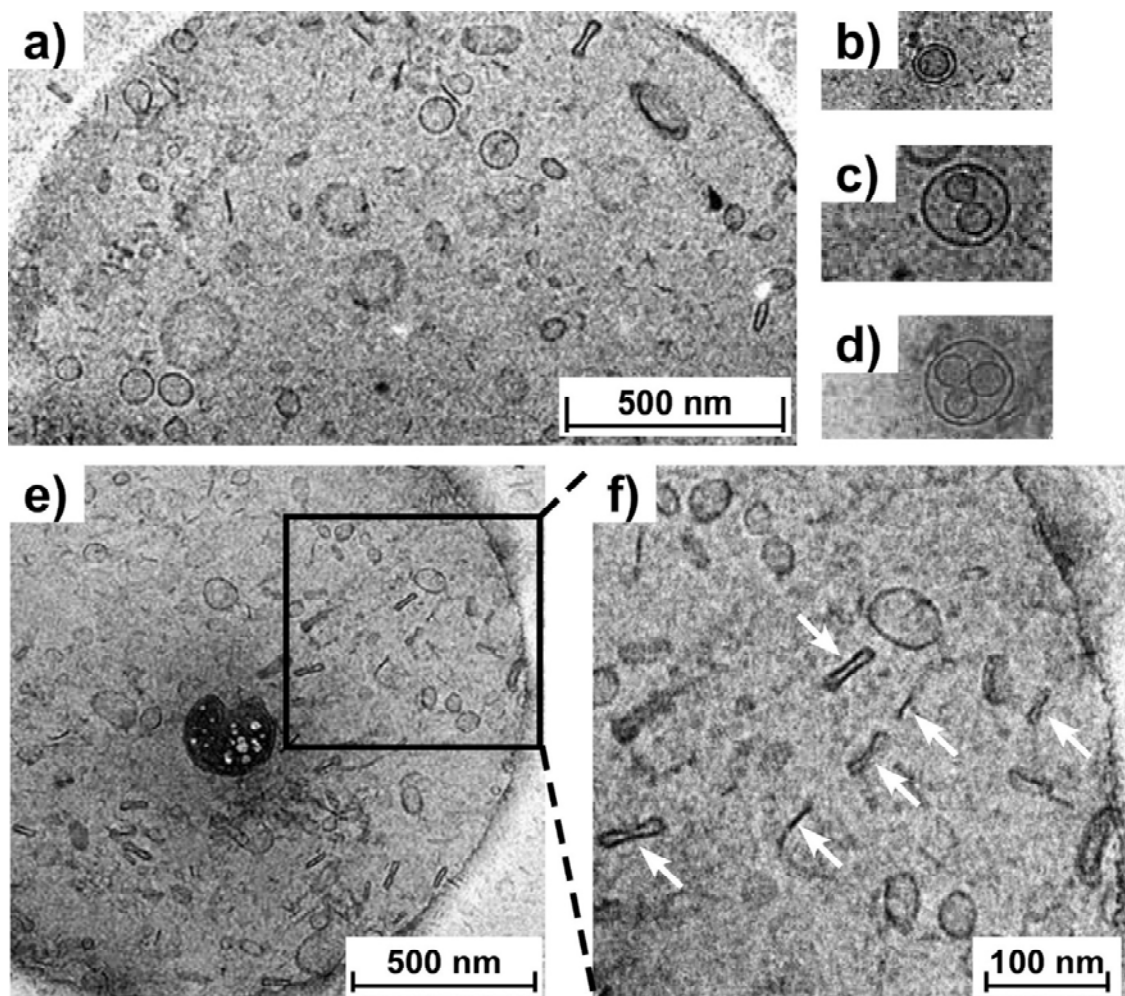


Figure 5.3. Cryo-TEM images of NERs. a) In isotonic solution, most NERs are unilamellar vesicles with sizes around 100 nm. In rare cases, NERs may also have two concentric membranes (b), or vesicle-in-vesicle structures: (c) and (d). NERs in hypertonic solution appear as biconcave structures: (e) and (f).

The previous cryo-TEM images were for NERs in DI water, and in this hypotonic environment, the NERs tend to swell. We also obtained cryo-TEM images for NERs in PBS buffer. In this environment, which is hypertonic in the case of the empty NERs, a majority of the NERs adopt a biconcave structure (Figure 5.3e, 5.3f). This is consistent with the known behavior of erythrocytes, which are biconcave in an isotonic medium, but swell into a more spherical geometry in hypotonic media. Note that between a biconcave disk and an equivalent sphere, the hydrodynamic diameter is expected to be identical, since D_h is dictated by the largest dimension of the object. This explains why similar D_h values were measured by DLS for the NERs in water and in PBS. The biconcave structure of the NERs can be clearly seen in the closeup image (Figure 5.3f). Note that, even after the micron-sized erythrocytes have been converted into nano-sized NERs, this biconcave structure is still retained! While the exact origin of biconcavity in erythrocytes is not established, it is generally attributed to the presence of a cytoskeletal network (made of the proteins spectrin and ankyrin) that is anchored to the bilayer membrane of the cells.⁹³ Presumably, this network is able to withstand the processing steps (osmotic shock and sonication) and remains intact in the NERs, giving them their characteristic shape.

We also studied NERs using SANS. For this, we prepared a pellet of the micron-sized erythrocytes as before and then suspended these in deuterium oxide (D_2O). This suspension was then sonicated to obtain the NERs. The use of D_2O ensures sufficient contrast between the scattering objects and the solvent under SANS. The scattered intensity I in SANS is measured as a function of the scattering vector q . For a dilute

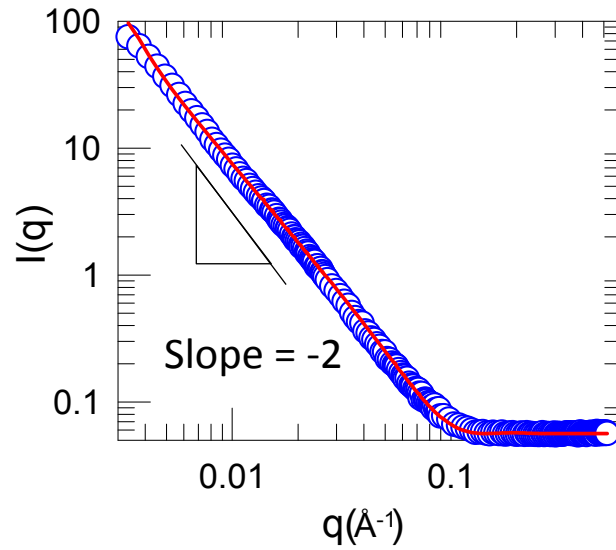


Figure 5.4. SANS spectra for NERs in D₂O. The intensity I follows a slope of -2 at low q , which is characteristic of unilamellar vesicles.

dispersion of weakly interacting vesicles, the intensity $I(q)$ can be accounted purely in terms of the form factor $P(q)$ of the scatterers (i.e., the structure factor $S(q) \rightarrow 1$). In turn, $I(q)$ is given by the following expression for the case where the vesicle radius R is large relative to the thickness t of the bilayer membrane:

$$I(q) \sim (4\pi R)^2 \cdot \frac{t^2}{q^2} \sin^2(qR) \quad (5.1)$$

Eq (5.1) indicates that $I(q)$ for such vesicles should show a q^{-2} decay in the low q range. SANS data are plotted in Figure 5.4 for NERs at a concentration of 18 mg/mL in D₂O. As expected, we find that the intensity I follows a slope of -2 at low and moderate q . Such a plot is indeed characteristic of unilamellar vesicles. (If the vesicles were multilamellar, we would see additional peak(s) at moderate q , corresponding to the interlamellar spacing.) The above SANS data is not sensitive to the overall size of the vesicles because

it falls outside the window of size scales probed by neutrons. However, it permits accurate estimation of the bilayer membrane thickness t . This value can be determined by plotting the data in a cross-sectional Guinier plot, i.e., a plot of $\ln(Iq^2)$ vs. q^2 , which yields a straight line with a slope = $t^2/12$ (this is equivalent to fitting eq 1 to the data). From this, we estimate $t \approx 4.5$ nm for the NERs. Our result matches with previous measurements of t for erythrocyte membranes, both human and animal, which have reported values of t around 4 nm.

Stability of NERs Compared to Liposomes

Our studies using SANS and cryo-TEM reveal that the structure of NERs is quite comparable to that of liposomes (both are unilamellar vesicles). Figure 5.2 also showed that the NERs are stable structures, i.e., they exhibit approximately the same size over several days. We now compare in more detail the stability of NERs against that of liposomes. First, we prepared conventional liposomes using the phospholipid DPPC and cholesterol. DPPC has two palmitoyl (C_{16} , saturated) tails and a zwitterionic phosphocholine headgroup. Since DPPC is zwitterionic and cholesterol is uncharged, DPPC/cholesterol liposomes have a negligible surface charge. Next, we prepared liposomes with PEG surface moieties by combining DPPC, cholesterol, and a third lipid, DOPE-mPEG. The latter has two oleyl (C_{18} , unsaturated) tails and an anionic phosphoethanol-amine headgroup attached to a PEG moiety of molecular weight 2000 Da. The anionic headgroups of DOPE-mPEG impart a net negative charge to the liposomes. We compare these with the NERs studied previously.

Figure 5.5a shows the normalized size of the three sets of structures over a period of time. Here, each sample is studied in the presence of serum, which is the solution component of blood that is rich in proteins and salts. Serum contains a variety of proteins, especially those that are a part of the immune system such as antibodies. The stability of nanostructures in serum is particularly important for drug-delivery applications. At time $t = 0$ in serum, all three structures had mean diameters around 100 nm, and this was also their diameter in aqueous buffer. The zeta potentials of the three in serum were measured to be 0.4 mV, -48 mV, and -38 mV, for the bare liposomes, PEGylated liposomes, and the NERs, respectively. Figure 5.5a shows that the bare liposomes are relatively unstable, with their size increasing by a factor of about 2.5 over the first 24 h in serum (this is indicative of aggregation into larger structures). Moreover, the liposome samples exhibited a precipitate at the bottom of the vial within 4 h of preparation. In comparison, both the PEGylated liposomes and the NERs remained stable (no change in size) over a period of 96 h. The higher stability of the latter two correlates with their more negative surface charge as well as the presence of steric-stabilizing moieties attached to the membrane. As mentioned, the stabilizing moieties in the case of the NERs are expected to be hydrophilic sugars attached to membrane proteins or lipids.

Another issue is the stability of nanostructures to freeze-thaw cycling. During freezing, ice crystals can form inside a liposome and the expansion of ice can rupture the membrane. When the sample is thawed, ideally the liposome should revert to its original size and structure. We subjected the three samples from above to a number of freeze-thaw cycles and measured their size at the end of each cycle. The results in Figure 5.5b

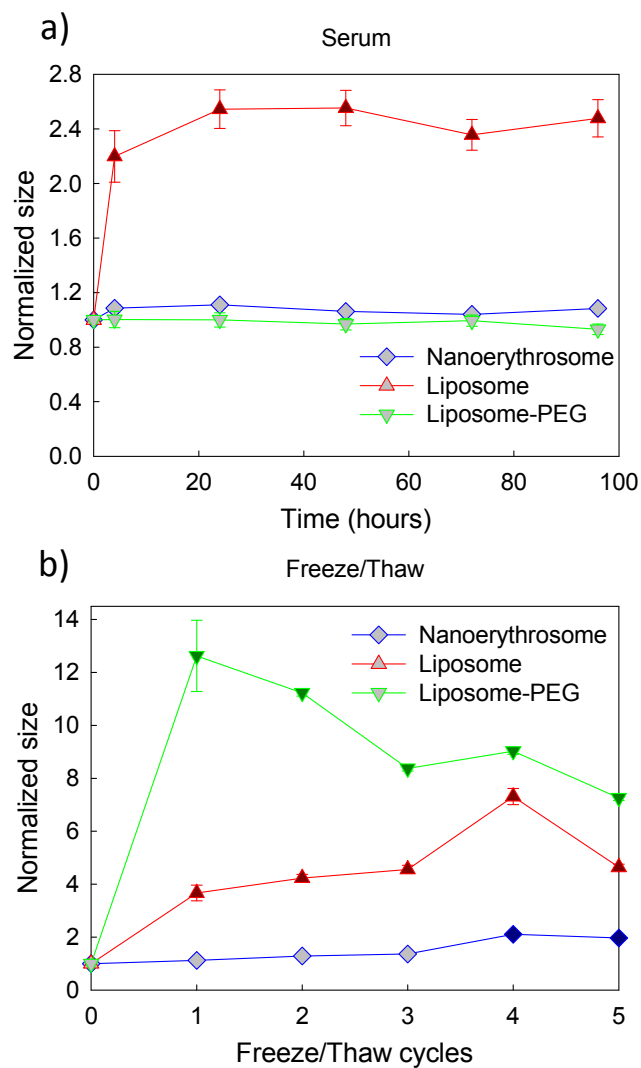


Figure 5.5. (a) Stability of NERs compared to liposomes or PEG-conjugated liposomes. (a) in serum; (b) in buffer, following freeze/thaw cycling. Filled points in (b) imply that the sample showed a precipitate.

reveal that the NERs are much more stable to freeze-thaw cycling than the bare or PEGylated liposomes. In the latter two cases, a precipitate was found in each sample after just one freeze-thaw cycle and the precipitation worsened with each such cycle. In the case of the NERs, only slight precipitation was found and that too only after 4 cycles.

Also, the size of the bare liposomes and PEGylated liposomes left in solution significantly increased upon freeze-thaw cycling, indicating aggregation, whereas the size of the NERs remained relatively constant even after 5 such cycles. We speculate that the presence of the spectrin-ankyrin filamentous network attached to the NER membrane is responsible for the greater stability of the NERs.

Solute Encapsulation in NERs and Subsequent Release

Liposomes are used in drug delivery because of their ability to encapsulate solutes in their aqueous interior and release them slowly into the external environment. We now examine whether similar solute encapsulation and release can be done with NERs. As a solute, we chose dextran-FITC, i.e., the polysaccharide dextran (molecular weight $\sim 4,000$ Da) attached to the fluorescent dye, fluorescein isothiocyanate (FITC). To encapsulate the solute in the NERs, we first added the solute to the erythrocyte suspension at room temperature and then sonicated the sample. The shear from sonication partially ruptures the erythrocyte membranes as they rearrange into NERs; during this process, some of the solute is internalized. We then subjected the sample to a temperature cycle (cool to 4°C , then warm to 37°C , then back to room temperature). During this process, the NER membranes are expected to get resealed.⁶² At this point, the NERs are loaded with solute, but free solute is also present in the external solution. To remove the free solute, the sample was purified through a size exclusion column. The resulting NERs have the solute only inside them, and this sample was then placed in a dialysis cassette (this point corresponds to $t = 0$ for the release experiments). We chose a dialysis membrane with a 12 kDa cutoff, which is sufficiently large to allow the dextran-FITC

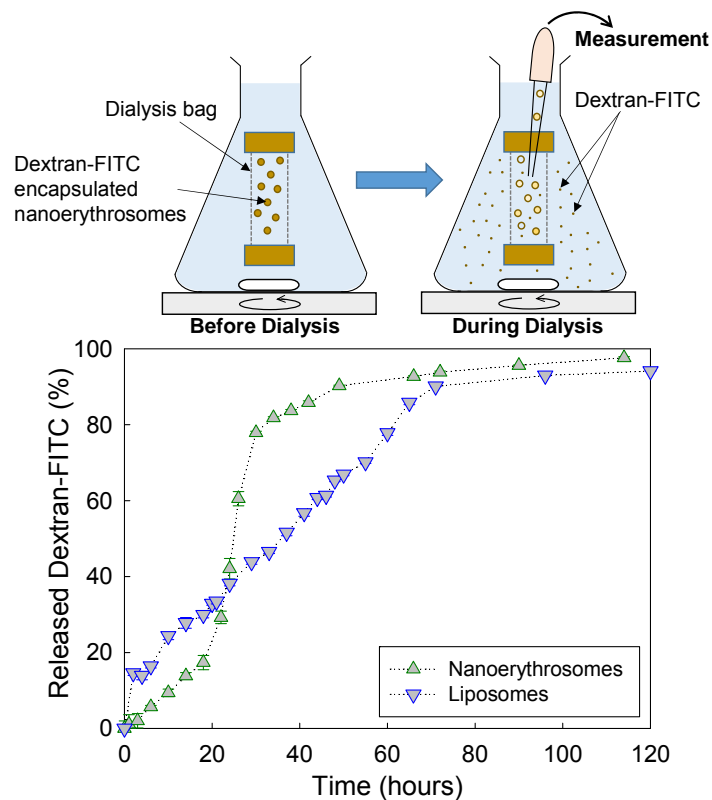


Figure 5.6. Release of solute (dextran-FITC) encapsulated in NERs or liposomes. The samples were placed in dialysis cassettes. The samples were dialyzed against excess of PBS buffer for more than four days at room temperature with constant stirring and buffer exchanges. Aliquots were withdrawn from the dialysis bag at various time points and analyzed for the concentration of solute.

solute to pass through it. Release of solute from the NERs to the external buffer solution was then monitored over time by periodically measuring the fluorescence of the solution in the dialysis cassette. For comparison with the NERs, a similar experiment was also done with liposomes of the phospholipid DPPC (diameter of ~ 100 nm).

Figure 5.6 shows release curves for dextran-FITC from the NERs and the liposomes. In the case of the liposomes, the release occurs at a nearly constant rate over the first 72 h and thereafter it slows down. In the case of the NERs, the release is slower

over the first 20 h, but then it picks up over the next 20 h, and finally, once about 80% of the solute is released, the rate of release slows down again. The NERs release < 10% of the solute over the first 10 h compared to the liposomes (~ 25% over the first 10 h). On the other hand, 90% of the solute is released by the NERs within 50 h compared to 75 h in the case of the liposomes. Note that a clean comparison between NERs and liposomes is not easy to make. While the NER sample contains about 3.2×10^{12} NERs/mL, the liposome sample has about 2×10^{12} liposomes/mL. While the same amount of solute was added to both samples at the outset, the encapsulation efficiencies of the two structures are also different. The total loading of dextran-FITC (from the readings as $t = 0$) was 40 $\mu\text{g/mL}$ in the NERs and 20 $\mu\text{g/mL}$ in the liposomes. Thus, the NERs encapsulate more of the solute, although the reason for this is not clear. Overall, we conclude from Figure 5.6 that NERs can also be used for solute release, much like the liposomes, and that the kinetics of solute release is comparable for the two cases.

Targeting Antibody-Conjugated NERs to Specific Cell Types

Many biomedical applications involve the use of immuno-liposomes, which have targeting agents such as antibodies conjugated to their external surface. Such structures can target and bind specifically to cells with receptors for the targeting agents (binding is usually followed by internalization into the cells through endocytosis). We wanted to examine whether such targeting could be carried out with surface-modified NERs. For this, we began with an anti-EGFR antibody, where EGFR refers to the epidermal growth factor receptor. We then added protein G, which is a protein that has the ability to bind to the constant (Fc) region of antibodies. Thereafter, we used an FDA-approved enzyme

called microbial transglutaminase (mTG) to conjugate the protein G-antibody complex to the membrane of the NERs. mTG is expected to create covalent bonds between the protein G portion and membrane proteins on the NERs. By this process, NERs modified with anti-EGFR antibodies were obtained, and these were further tagged with a red-fluorescent lipid, DiI to aid in visualization.

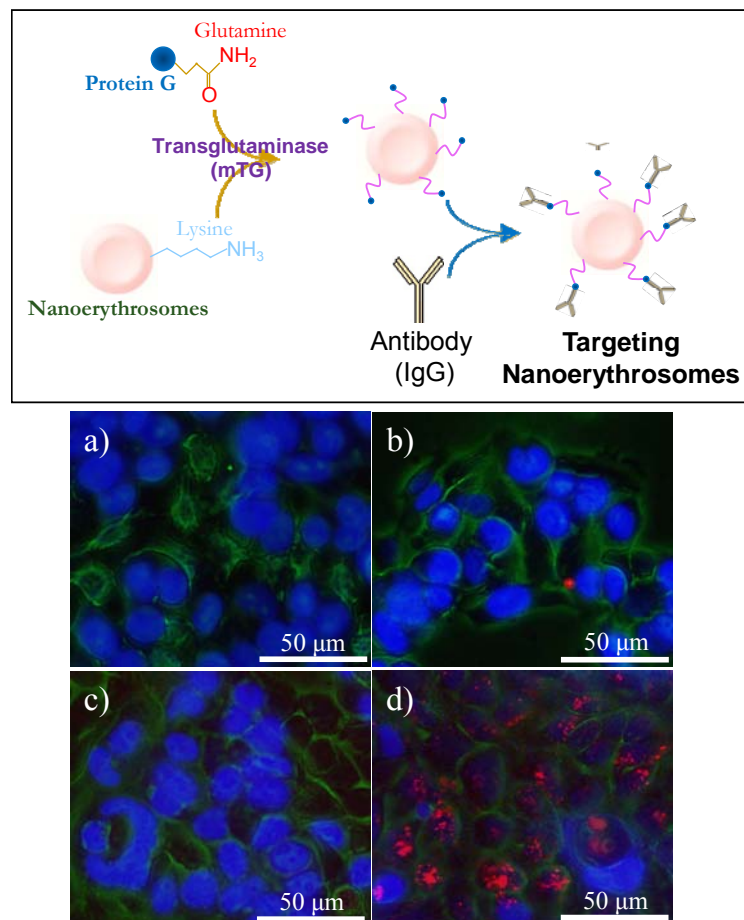


Figure 5.7. Attachment of targeting moieties to NERs, and evaluation of their targeting affinity. (Top) Schematic of mTG-mediated conjugation of protein G via glutamine to lysine on NERs, followed by spontaneous binding of protein G to the stem of antibodies. (Bottom) Fluorescence micrographs of 15B cells (which overexpress EGFR) incubated with a) blank, b) liposomes, c) NERs with protein G-IgG_{2a}, d) NERs with protein G-anti-EGFR. Green represents cell boundaries, blue is DAPI counterstain of nuclei, and red indicates the nanostructures.

We then selected the 15B cell line, which is a class of squamous cell carcinoma of the head and neck (SCCHN). These cells are known to over-express EGFRs on their membranes. The cells and the above NERs were incubated for 30 min, followed by washing to remove unbound structures. As a control, we also synthesized NERs with a different antibody (mouse IgG_{2a}) that has no affinity for EGFR using the same procedure as above. Figure 5.7 shows images from fluorescence microscopy for the two cases. The NERs with anti-EGFR antibodies show substantial binding to the 15B cells as seen by the significant red fluorescence. In the control case, there is negligible binding of the NERs to the 15B cells, as noted from the absence of red fluorescence. These results indicate that NERs tagged with antibodies can serve as targeting agents, with the ability to bind to specific types of cells. Thus, we again show that NERs can have many of the same functions and capabilities as liposomes.

5.4. Conclusions

In this study, we extracted erythrocytes from bovine blood and converted these into nanoerythrocytes (NERS). This was done by using osmotic gradients to remove the hemoglobin, and then sonicating the empty structures. NERS were found to be nanospheres with an average diameter ~ 110 nm, enclosed by a unilamellar bilayer membrane of thickness ~ 4.5 nm. Compared to liposomes, NERS show improved colloidal stability in buffer and in serum, and are more stable to freeze-thaw cycling. Much like liposomes, NERS can encapsulate solutes (small molecules or macromolecules) in their aqueous core, and these can be subsequently released by diffusion through the bilayer. NERS can also be decorated with targeting agents like antibodies, and such NERS can bind specifically to cells that have the receptors for the antibodies. In other words, NERS have many of the same capabilities as conventional liposomes, but with the added advantage of better colloidal stability. This improved stability is evidently because many of the membrane proteins and glycolipids attached to the blood cell membrane are still intact in the case of the NERS. While the presence of these membrane-bound molecules is beneficial in this context, there is also the risk of an immune response to these molecules if NERS were injected into a foreign species. However, there is the possibility of harvesting NERS from a patient's own blood. This possibility can become more realistic if NER preparation and functionalization can be performed at the bedside, possibly using lab-on-a-chip devices. Such NERS may potentially offer several benefits including biocompatibility, minimization of immune response, and most importantly, an extended circulation time in the body.

Chapter 6

Conclusions and Recommendations

6.1. Project Summary and Principal Contributions

In this dissertation, we have shown three kinds of delivery carriers which specifically recognized head & neck cancer cells. These carriers were developed from biocompatible materials with a simple purification process and minimal chemical reactions to facilitate scale-up toward clinical usage. The carrier sources come from either biomimetic (liposomes – chapter 3) or natural cells (microerythrocytes – chapter 4, nanoerythrocytes – chapter 5). An EGFR antibody (Cetuximab) was conjugated onto these carriers through a non-covalent or enzymatic method to provide targeting ability for drug delivery.

In chapter 3, we described a simple self-assembled liposomal nanocarrier with the ability to bind to head & neck cancer cells and display a MRI signal. The construct was first formed by DPPC liposomes with MRI contrast (Gd) using a sonication method followed by conjugation of EGFR antibody (Cetuximab) to the surface. The nanocarriers have a size of 100 nm and show significant stability over two weeks. The stable construct can selectively deliver contrast agent to 15B cells with significant MRI contrast as displayed in an *in vitro* study for tracking cancer localization.

In Chapter 4, we reported a natural carrier based on red blood cells (RBCs) called

micro erythrocytes (MERs). These MERs display advantages inherited from RBCs, including biocompatibility and long term stability. Additionally, the MERs sacrifice their contents (e.g. hemoglobins and proteins) to accept therapeutic agents or drugs, which allows more agent to be stored within the MER than if a RBC alone was loaded with the agent. Furthermore, MERs can be created from a patient's own blood to yield a personalized treatment. Finally, MER membranes, unlike RBCs, are easily functionalized, which converts MERs into multifunctional carriers. As a result, the MERs display the ability to selectively deliver MRI contrast agent to head & neck cancer cells.

In Chapter 5, we demonstrate the practical application of biomimetic nanocarriers derived from RBCs, which are further processed from MERs to yield a nano-sized carrier, nanoerythrocytes (NERs). The NERs have a strong skeletal system to maintain their structures in a sphere or biconcave structure, and tolerate various deformations. In order to minimize toxicity the binding of a targeting antibody to NERs is also processed with microbial transglutaminase (mTG), which is FDA approved. Surface functionalized NERs also display the ability to encapsulate drug and specifically deliver it to head & neck cancer cells in a similar manner to our previously studied ERs. Additionally, NERs have a size advantage over MERs displayed by the fact that NERs can accumulate and penetrate local areas of tissue due to their smaller size.

We believe the introduction of the above simple, enzymatic formulation of biomimetic and natural carrier development will replace the high cost and low biocompatibility manufacture of current drug delivery products, and be beneficial in the

field of personalized drug delivery systems.

6.2. Recommendations for Future Work

The work we have done in this dissertation can be further extended and explored for more detail and new applications. The following is the recommendations for the future work.

6.2.1 Control release of drugs

In this dissertation, we reported drug release rate for different carriers; the stronger barrier, the slower release rate. It could be possible to elongate the drug release time by adjusting the lipid ratio for vesicle, or incorporating the crosslinking on the membrane to slow the leak. However, it is difficult to accurately control the membrane permeability and the stability, especially the natural material. For the drug delivery aspect, sometimes the release timing could be an even critical factor for the drug efficiency. Recently, a group of second-messenger molecules, which regulated intracellular signaling pathways, shows to involve in many physiological and pathological processes. One example is dipalmitoylphosphatidylcholine (DPPC). DPPC is hydrolyzed by the enzyme phospholipase A₂ (PLA₂) at the ester bond of glycerol phospholipids at the C₂ carbon,

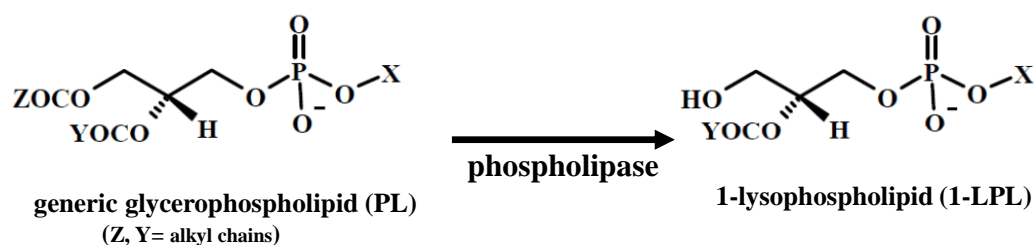


Figure 6.1. Structures of phospholipid and derivative. One acyl chain is removed from phospholipid by phospholipase and generates lysophospholipid.

and produces two secondary-messenger molecules: palmitoyl-lyso-phosphatidyl choline (LPC) and palmitic acid (PA), in a 1:1 molar ratio (Figure 6.1).⁹⁴ Compared to the LPC (lysophospholipid), phospholipid tends to form lamellar vesicle, but lysophospholipid is similar to surfactant, which may form micelle. Lysophospholipid has been proved that it can be used to achieve local mild hyperthermia in tumor and impact drug delivery systems due to the sensitivity of low temperature.^{95,96} As the temperature raising process, the liposome may become more porous property to release the drug, and that could be an effective control release switch for our lipid formulated erythroosome/nanoerythroosome model.

6.2.2 Specific clearance of cancers

To further evaluate the drug delivery with cancer clearance functionality for MER or NER, we can encapsulate some anticancer drug or potential killing reagent in the core of them, for example, glucose oxidase (GOx). The glucose oxidase is a commercial available enzyme that catalyzes glucose into hydrogen peroxide (H_2O_2) and gluconic acid (Figure 6.2a). Hydrogen peroxide may damage cells through direct oxidation of lipids,

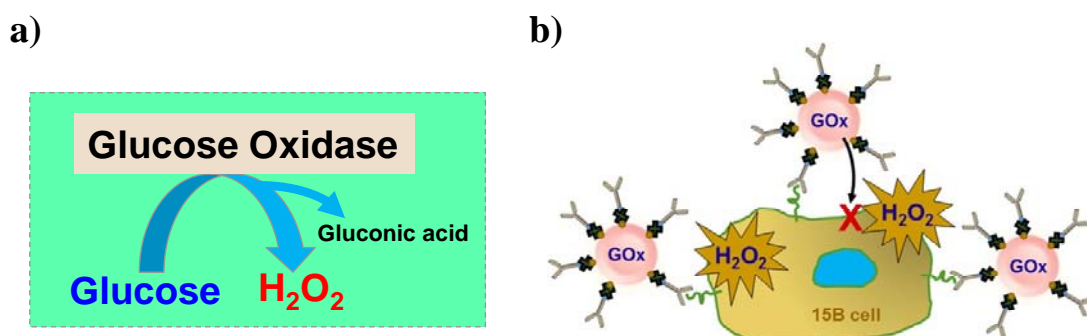


Figure 6.2. Glucose oxidase commonly used on food market. a) Glucose oxidase can convert glucose into gluconic acid and hydrogen peroxide, b) once the targeted MERs attach to the surface of cells, then the product of enzyme may kill cells by hydrogen peroxide.

proteins and DNA or it can act as a signaling molecule to trigger intracellular pathways leading to cell death.^{97,98} By adapting the similar platform from chapter 4, we can encapsulate GOx easily in MERs with resealing method. 15B cells as high EGFR expression model are seeded in a 96-wells plate, and incubated with either control MERs without targeting function, or the MER probes, both containing glucose oxidase. After short incubation time, the unbind MERs should be washed off from the cells and the MERs which still bind to the cells will begin to generate hydrogen peroxide by catalyzing the glucose in medium. Once the localized concentration is high enough, then the cell membrane may get damage or even lethal for the cells. By encapsulating the glucose oxidase with the targeting MERs, it may turn the biocompatible carrier into a cancer clearance agent (Figure 6.2b).

6.2.3 Animal studies

Studies in a wide range of animals were foundational and critical for understanding the potential impact to human. Particularly, the animal testing helps to ensure the safety of carriers/drugs and many other substances. Some of the drugs may only show the dangerous effect when combining with the metabolism in the body, while the *in vitro* would not show the toxicity. For the treatment aspect, carriers/drugs may be sensitive to the temperature, pH and immune cells in the circulation system, these animal studies will further exam for the essential characteristics of our products. That means that between *in vitro* and clinical studies, it's necessary for testing our system with animal studies *in vivo*, which can contribute to the reduced human harm and improve the quality of human life.

7. References

- [1] Weissleder, R.; Pittet, M. J. "Imaging in the era of molecular oncology." *Nature* **2008**, *452*, 580-9.
- [2] Darras, V.; Nelea, M.; Winnik, F. M.; Buschmann, M. D. "Chitosan modified with gadolinium diethylenetriaminepentaacetic acid for magnetic resonance imaging of DNA/chitosan nanoparticles." *Carbohydrate Polymers* **2010**, *80*, 1137-1146.
- [3] Fujimoto, T.; Ichikawa, H.; Akisue, T.; Fujita, I.; Kishimoto, K.; Hara, H.; Imabori, M.; Kawamitsu, H.; Sharma, P.; Brown, S. C.; Moudgil, B. M.; Fujii, M.; Yamamoto, T.; Kurosaka, M.; Fukumori, Y. "Accumulation of MRI contrast agents in malignant fibrous histiocytoma for gadolinium neutron capture therapy." *Appl Radiat Isot* **2009**, *67*, S355-8.
- [4] Nam, T.; Park, S.; Lee, S. Y.; Park, K.; Choi, K.; Song, I. C.; Han, M. H.; Leary, J. J.; Yuk, S. A.; Kwon, I. C.; Kim, K.; Jeong, S. Y. "Tumor targeting chitosan nanoparticles for dual-modality optical/MR cancer imaging." *Bioconjug Chem* **2010**, *21*, 578-82.
- [5] Kim, E. S.; Khuri, F. R.; Herbst, R. S. "Epidermal growth factor receptor biology (IMC-C225)." *Current opinion in oncology* **2001**, *13*, 506-13.
- [6] Baumann, M.; Krause, M. "Targeting the epidermal growth factor receptor in radiotherapy: radiobiological mechanisms, preclinical and clinical results." *Radiother Oncol* **2004**, *72*, 257-66.
- [7] Harari, P. M.; Huang, S. M. "Epidermal growth factor receptor inhibition in cancer therapy: Biology, rationale and preliminary clinical results." *Investigational New Drugs* **1999**, *17*, 259-269.
- [8] Frampton, J. E. "Cetuximab A Review of its Use in Squamous Cell Carcinoma of the Head and Neck." *Drugs* **2010**, *70*, 1987-2010.
- [9] Bonner, J. A.; Harari, P. M.; Giralt, J.; Cohen, R. B.; Jones, C. U.; Sur, R. K.; Raben, D.; Baselga, J.; Spencer, S. A.; Zhu, J.; Youssoufian, H.; Rowinsky, E. K.; Ang, K. K. "Radiotherapy plus cetuximab for locoregionally advanced head and neck cancer: 5-year survival data from a phase 3 randomised trial, and relation between cetuximab-induced rash and survival." *Lancet Oncol* **2010**, *11*, 21-8.

- [10] Vermorken, J. B.; Mesia, R.; Rivera, F.; Remenar, E.; Kawecki, A.; Rottey, S.; Erfan, J.; Zabolotnyy, D.; Kienzer, H. R.; Cupissol, D.; Peyrade, F.; Benasso, M.; Vynnychenko, I.; De Raucourt, D.; Bokemeyer, C.; Schueler, A.; Amellal, N.; Hitt, R. "Platinum-based chemotherapy plus cetuximab in head and neck cancer." *New England Journal of Medicine* **2008**, *359*, 1116-1127.
- [11] Carty, F.; Shortt, C. P.; Shelly, M. J.; Eustace, S. J.; O'Connell, M. J. "Whole-body imaging modalities in oncology." *Semin Musculoskelet Radiol* **2010**, *14*, 68-85.
- [12] Pautler, R. G. "Mouse MRI: Concepts and applications in physiology." *Physiology* **2004**, *19*, 168-175.
- [13] Singh, N.; Jenkins, G. J. S.; Asadi, R.; Doak, S. H. "Potential toxicity of superparamagnetic iron oxide nanoparticles (SPION)." *Nano Reviews* **2010**, *1*.
- [14] Pashkunova-Martic, I.; Kremser, C.; Galanski, M.; Arion, V.; Debbage, P.; Jaschke, W.; Keppler, B. "Lectin-Gd-loaded chitosan hydrogel nanoparticles: a new biospecific contrast agent for MRI." *Mol Imaging Biol* **2011**, *13*, 16-24.
- [15] Petersen, S.; Mohrs, O.; Horstick, G.; Oberholzer, K.; Abegunewardene, N.; Ruetzel, K.; Selvanayagam, J.; Robson, M.; Neubauer, S.; Thelen, M.; Meyer, J.; Kreitner, K. F. "Influence of Contrast Agent Dose and Image Acquisition Timing on the Quantitative Determination of Nonviable Myocardial Tissue Using Delayed Contrast-Enhanced Magnetic Resonance Imaging." *Journal of Cardiovascular Magnetic Resonance* **2004**, *6*, 541-548.
- [16] Sherry, A. D.; De Leon-Rodriguez, L. M.; Lubag, A. J. M.; Malloy, C. R.; Martinez, G. V.; Gillies, R. J. "Responsive MRI Agents for Sensing Metabolism in Vivo." *Accounts of Chemical Research* **2009**, *42*, 948-957.
- [17] Cowper, S. E.; Kuo, P. H.; Bucala, R. "Nephrogenic systemic fibrosis and gadolinium exposure: association and lessons for idiopathic fibrosing disorders." *Arthritis Rheum* **2007**, *56*, 3173-5.
- [18] Bellin, M. F. "MR contrast agents, the old and the new." *Eur J Radiol* **2006**, *60*, 314-23.
- [19] Evans, D. F.; Wennerström, H. k. *The colloidal domain : where physics, chemistry, biology, and technology meet*; Wiley-VCH: New York, 1999.
- [20] Lasic, D. D. *Liposomes : from physics to applications*; Elsevier: Amsterdam; New York, 1993.

- [21] Kaler, E. W.; Murthy, A. K.; Rodriguez, B. E.; Zasadzinski, J. A. N. "Spontaneous Vesicle Formation in Aqueous Mixtures of Single-Tailed Surfactants." *Science* **1989**, *245*, 1371-1374.
- [22] Israelachvili, J. N. 21 - Interactions of Biological Membranes and Structures. In *Intermolecular and Surface Forces (Third Edition)*; Israelachvili, J. N., Ed.; Academic Press: San Diego, 2011; pp 577-616.
- [23] Brown, W. *Dynamic light scattering : the method and some applications*; Clarendon Press ; Oxford University Press: Oxford [England]; New York, 1993.
- [24] Bast, R. C., Jr.; Boyer, C. M.; Jacobs, I.; Xu, F. J.; Wu, S.; Wiener, J.; Kohler, M.; Berchuck, A. "Cell growth regulation in epithelial ovarian cancer." *Cancer* **1993**, *71*, 1597-601.
- [25] Ishikawa, J.; Maeda, S.; Umezu, K.; Sugiyama, T.; Kamidono, S. "Amplification and overexpression of the epidermal growth factor receptor gene in human renal-cell carcinoma." *Int J Cancer* **1990**, *45*, 1018-21.
- [26] Kim, J. W.; Kim, Y. T.; Kim, D. K.; Song, C. H.; Lee, J. W. "Expression of epidermal growth factor receptor in carcinoma of the cervix." *Gynecol Oncol* **1996**, *60*, 283-7.
- [27] Rikimaru, K.; Tadokoro, K.; Yamamoto, T.; Enomoto, S.; Tsuchida, N. "Gene amplification and overexpression of epidermal growth factor receptor in squamous cell carcinoma of the head and neck." *Head Neck* **1992**, *14*, 8-13.
- [28] Robertson, K. W.; Reeves, J. R.; Smith, G.; Keith, W. N.; Ozanne, B. W.; Cooke, T. G.; Stanton, P. D. "Quantitative estimation of epidermal growth factor receptor and c-erbB-2 in human breast cancer." *Cancer Res* **1996**, *56*, 3823-30.
- [29] Mukherjee, B.; McEllin, B.; Camacho, C. V.; Tomimatsu, N.; Sirasanagandala, S.; Nannepaga, S.; Hatanpaa, K. J.; Mickey, B.; Madden, C.; Maher, E.; Boothman, D. A.; Furnari, F.; Cavenee, W. K.; Bachoo, R. M.; Burma, S. "EGFRvIII and DNA double-strand break repair: a molecular mechanism for radioresistance in glioblastoma." *Cancer Res* **2009**, *69*, 4252-9.
- [30] Liang, Z.; Zhang, J.; Zeng, X.; Gao, J.; Wu, S.; Liu, T. "Relationship between EGFR expression, copy number and mutation in lung adenocarcinomas." *BMC Cancer* **2010**, *10*, 376.
- [31] Pattje, W. J.; Schuurin, E.; Mastik, M. F.; Slagter-Menkema, L.; Schrijvers, M. L.; Alessi, S.; van der Laan, B. F.; Roodenburg, J. L.; Langendijk, J. A.; van der Wal, J. E. "The

- phosphatase and tensin homologue deleted on chromosome 10 mediates radiosensitivity in head and neck cancer." *Br J Cancer* **2010**, *102*, 1778-85.
- [32] Volkel, T.; Holig, P.; Merdan, T.; Muller, R.; Kontermann, R. E. "Targeting of immunoliposomes to endothelial cells using a single-chain Fv fragment directed against human endoglin (CD105)." *Biochim Biophys Acta* **2004**, *1663*, 158-66.
- [33] Jonker, D. J.; O'Callaghan, C. J.; Karapetis, C. S.; Zalcborg, J. R.; Tu, D.; Au, H. J.; Berry, S. R.; Krahn, M.; Price, T.; Simes, R. J.; Tebbutt, N. C.; van Hazel, G.; Wierzbicki, R.; Langer, C.; Moore, M. J. "Cetuximab for the treatment of colorectal cancer." *N Engl J Med* **2007**, *357*, 2040-8.
- [34] Grobner, T.; Prischl, F. C. "Gadolinium and nephrogenic systemic fibrosis." *Kidney Int* **2007**, *72*, 260-4.
- [35] Weinmann, H. J.; Brasch, R. C.; Press, W. R.; Wesbey, G. E. "Characteristics of gadolinium-DTPA complex: a potential NMR contrast agent." *AJR Am J Roentgenol* **1984**, *142*, 619-24.
- [36] Luo, K.; Liu, G.; She, W.; Wang, Q.; Wang, G.; He, B.; Ai, H.; Gong, Q.; Song, B.; Gu, Z. "Gadolinium-labeled peptide dendrimers with controlled structures as potential magnetic resonance imaging contrast agents." *Biomaterials* **2011**, *32*, 7951-60.
- [37] Luo, K.; Liu, G.; He, B.; Wu, Y.; Gong, Q.; Song, B.; Ai, H.; Gu, Z. "Multifunctional gadolinium-based dendritic macromolecules as liver targeting imaging probes." *Biomaterials* **2011**, *32*, 2575-85.
- [38] Luo, K.; Liu, G.; Zhang, X.; She, W.; He, B.; Nie, Y.; Li, L.; Wu, Y.; Zhang, Z.; Gong, Q.; Gao, F.; Song, B.; Ai, H.; Gu, Z. "Functional L-lysine dendritic macromolecules as liver-imaging probes." *Macromol Biosci* **2009**, *9*, 1227-36.
- [39] Chen, H. T.; Neerman, M. F.; Parrish, A. R.; Simanek, E. E. "Cytotoxicity, hemolysis, and acute in vivo toxicity of dendrimers based on melamine, candidate vehicles for drug delivery." *Journal of the American Chemical Society* **2004**, *126*, 10044-8.
- [40] Ghaghada, K. B.; Ravoori, M.; Sabapathy, D.; Bankson, J.; Kundra, V.; Annapragada, A. "New dual mode gadolinium nanoparticle contrast agent for magnetic resonance imaging." *PLoS One* **2009**, *4*, e7628.
- [41] Woodle, M. C.; Collins, L. R.; Sponsler, E.; Kossovsky, N.; Papahadjopoulos, D.; Martin, F. J. "Sterically stabilized liposomes. Reduction in electrophoretic mobility but not electrostatic surface potential." *Biophys J* **1992**, *61*, 902-10.

- [42] Caravan, P. "Strategies for increasing the sensitivity of gadolinium based MRI contrast agents." *Chem Soc Rev* **2006**, *35*, 512-23.
- [43] Ye, M.; Qian, Y.; Tang, J.; Hu, H.; Sui, M.; Shen, Y. "Targeted biodegradable dendritic MRI contrast agent for enhanced tumor imaging." *J Control Release* **2013**.
- [44] Cheng, Z.; Thorek, D. L.; Tsourkas, A. "Gadolinium-conjugated dendrimer nanoclusters as a tumor-targeted T1 magnetic resonance imaging contrast agent." *Angew Chem Int Ed Engl* **2010**, *49*, 346-50.
- [45] Grandis, J. R.; Tweardy, D. J. "Elevated levels of transforming growth factor alpha and epidermal growth factor receptor messenger RNA are early markers of carcinogenesis in head and neck cancer." *Cancer Res* **1993**, *53*, 3579-84.
- [46] Kalyankrishna, S.; Grandis, J. R. "Epidermal growth factor receptor biology in head and neck cancer." *Journal of Clinical Oncology* **2006**, *24*, 2666-72.
- [47] van Leeuwen, J. E. M.; Alwan, H. A. J. "UBPY-mediated epidermal growth factor receptor (EGFR) de-ubiquitination promotes EGFR degradation." *Journal of Biological Chemistry* **2007**, *282*, 1658-1669.
- [48] Luo, W. J.; Zhang, Y. M.; Li, X.; Xu, X. M. "Construction of a high-EGFR expression cell line and its biological properties comparing with A431 cell." *African Journal of Biotechnology* **2010**, *9*, 4674-4680.
- [49] Fillion, M. C.; Phillips, N. C. "Toxicity and immunomodulatory activity of liposomal vectors formulated with cationic lipids toward immune effector cells." *Biochim Biophys Acta* **1997**, *1329*, 345-56.
- [50] Smistad, G.; Jacobsen, J.; Sande, S. A. "Multivariate toxicity screening of liposomal formulations on a human buccal cell line." *Int J Pharm* **2007**, *330*, 14-22.
- [51] Mulder, W. J.; Strijkers, G. J.; Griffioen, A. W.; van Bloois, L.; Molema, G.; Storm, G.; Koning, G. A.; Nicolay, K. "A liposomal system for contrast-enhanced magnetic resonance imaging of molecular targets." *Bioconjug Chem* **2004**, *15*, 799-806.
- [52] Bangham, A. D.; Horne, R. W. "Negative Staining of Phospholipids and Their Structural Modification by Surface-Active Agents as Observed in the Electron Microscope." *J Mol Biol* **1964**, *8*, 660-8.

- [53] Huang, C. "Studies on phosphatidylcholine vesicles. Formation and physical characteristics." *Biochemistry* **1969**, *8*, 344-52.
- [54] Arthurs, G. "Carbon dioxide transport." *Continuing Education in Anaesthesia, Critical Care & Pain* **2005**, *5*, 207-210.
- [55] Cuppoletti, J.; Mayhew, E.; Zobel, C. R.; Jung, C. Y. "Erythroosomes - Large Proteoliposomes Derived from Crosslinked Human-Erythrocyte Cytoskeletons and Exogenous Lipid." *Proceedings of the National Academy of Sciences of the United States of America-Biological Sciences* **1981**, *78*, 2786-2790.
- [56] Mangal, P. C.; Kaur, A. "Electroporation of Red-Blood-Cell Membrane and Its Use as a Drug Carrier System." *Indian Journal of Biochemistry & Biophysics* **1991**, *28*, 219-221.
- [57] Harisa, G. I.; Ibrahim, M. F.; Alanazi, F.; Shazly, G. A. "Engineering erythrocytes as a novel carrier for the targeted delivery of the anticancer drug paclitaxel." *Saudi Pharmaceutical Journal* **2014**, *22*, 223-230.
- [58] Kim, S. H.; Kim, E. J.; Hou, J. H.; Kim, J. M.; Choi, H. G.; Shim, C. K.; Oh, Y. K. "Opsonized erythrocyte ghosts for liver-targeted delivery of antisense oligodeoxynucleotides." *Biomaterials* **2009**, *30*, 959-67.
- [59] Millan, C. G.; Castaneda, A. Z.; Marinero, M. L. S.; Lanao, J. M. "Factors associated with the performance of carrier erythrocytes obtained by hypotonic dialysis." *Blood Cells Molecules and Diseases* **2004**, *33*, 132-140.
- [60] Frame, T.; Carroll, T.; Korchagina, E.; Bovin, N.; Henry, S. "Synthetic glycolipid modification of red blood cell membranes." *Transfusion* **2007**, *47*, 876-82.
- [61] Omran, A. A. "Equilibrium thermodynamics of the partitioning of non-steroidal anti-inflammatory drugs into human erythrocyte ghost membranes." *Journal of Chemical Thermodynamics* **2013**, *66*, 9-13.
- [62] Sternberg, N.; Georgieva, R.; Duft, K.; Baumler, H. "Surface-modified loaded human red blood cells for targeting and delivery of drugs." *Journal of Microencapsulation* **2012**, *29*, 9-20.
- [63] Subra, C.; Laulagnier, K.; Perret, B.; Record, M. "Exosome lipidomics unravels lipid sorting at the level of multivesicular bodies." *Biochimie* **2007**, *89*, 205-212.

- [64] Huwlyer, J.; Wu, D. F.; Pardridge, W. M. "Brain drug delivery of small molecules using immunoliposomes." *Proceedings of the National Academy of Sciences of the United States of America* **1996**, *93*, 14164-14169.
- [65] Hong, J. S.; Vreeland, W. N.; Lacerda, S. H.; Locascio, L. E.; Gaitan, M.; Raghavan, S. R. "Liposome-templated supramolecular assembly of responsive alginate nanogels." *Langmuir* **2008**, *24*, 4092-6.
- [66] Lee, J. H.; Oh, H.; Baxa, U.; Raghavan, S. R.; Blumenthal, R. "Biopolymer-Connected Liposome Networks as Injectable Biomaterials Capable of Sustained Local Drug Delivery." *Biomacromolecules* **2012**, *13*, 3388-3394.
- [67] Kuo, Y. C.; Hung, C. W.; Gullapalli, R. P.; Xu, S.; Zhuo, J. C.; Raghavan, S. R.; D'Souza, W. D. "Liposomal nanoprobe that combine anti-EGFR antibodies and MRI contrast agents: synthesis and in vitro characterization." *Rsc Advances* **2014**, *4*, 33756-33764.
- [68] Torchilin, V. P. "Recent advances with liposomes as pharmaceutical carriers." *Nature Reviews Drug Discovery* **2005**, *4*, 145-160.
- [69] Rongen, H. A. H.; Bult, A.; vanBennekom, W. P. "Liposomes and immunoassays." *Journal of Immunological Methods* **1997**, *204*, 105-133.
- [70] Nobs, L.; Buchegger, F.; Gurny, R.; Allemann, E. "Current methods for attaching targeting ligands to liposomes and nanoparticles." *Journal of Pharmaceutical Sciences* **2004**, *93*, 1980-1992.
- [71] Collins, D.; Connor, J.; Tingbeall, H. P.; Huang, L. "Proton and Divalent-Cations Induce Synergistic but Mechanistically Different Destabilizations of Ph-Sensitive Liposomes Composed of Dioleoyl Phosphatidylethanolamine and Oleic-Acid." *Chemistry and Physics of Lipids* **1990**, *55*, 339-349.
- [72] Pouliot, R.; Saint-Laurent, A.; Chypre, C.; Audet, R.; Vitte-Mony, I.; Gaudreault, R. C.; Auger, M. "Spectroscopic characterization of nanoErythroosomes in the absence and presence of conjugated polyethyleneglycols: an FTIR and ³¹P-NMR study." *Biochim Biophys Acta* **2002**, *1564*, 317-24.
- [73] Woodle, M. C.; Lasic, D. D. "Sterically stabilized liposomes." *Biochimica Et Biophysica Acta* **1992**, *1113*, 171-199.
- [74] Allen, T. M. "Long-circulating (sterically stabilized) liposomes for targeted drug-delivery." *Trends in Pharmacological Sciences* **1994**, *15*, 215-220.

- [75] Moghimi, S. M.; Szabeni, J. "Stealth liposomes and long circulating nanoparticles: critical issues in pharmacokinetics, opsonization and protein-binding properties." *Progress in Lipid Research* **2003**, *42*, 463-478.
- [76] Jones, M. N.; Nicholas, A. R. "The effect of blood-serum on the size and stability of phospholipid liposomes." *Biochimica Et Biophysica Acta* **1991**, *1065*, 145-152.
- [77] Wyrwal, M.; Bednar, J.; Nowakowska, M.; Wydro, P.; Kepczynski, M. "Interactions of serum with polyelectrolyte-stabilized liposomes: Cryo-TEM studies." *Colloids and Surfaces B-Biointerfaces* **2014**, *120*, 152-159.
- [78] Yadava, P.; Gibbs, M.; Castro, C.; Hughes, J. A. "Effect of lyophilization and freeze-thawing on the stability of siRNA-liposome complexes." *Aaps Pharmscitech* **2008**, *9*, 335-341.
- [79] Alachi, A.; Boroujerdi, M. "Pharmacokinetics and Tissue Uptake of Doxorubicin Associated with Erythrocyte-Membrane - Erythrocyte-Ghosts Vs Erythrocyte-Vesicles." *Drug Development and Industrial Pharmacy* **1990**, *16*, 2199-2219.
- [80] Al-Achi, A.; Greenwood, R. "Erythrocytes as oral delivery systems for human insulin." *Drug Development and Industrial Pharmacy* **1998**, *24*, 67-72.
- [81] Lejeune, A.; Moorjani, M.; Gicquaud, C.; Lacroix, J.; Poyet, P.; Gaudreault, R. "Nanoerythroosome, a new derivative of erythrocyte ghost: preparation and antineoplastic potential as drug carrier for daunorubicin." *Anticancer Res* **1994**, *14*, 915-9.
- [82] Lejeune, A.; Poyet, P.; Gaudreault, R. C.; Gicquaud, C. "Nanoerythroosomes, a new derivative of erythrocyte ghost: III. Is phagocytosis involved in the mechanism of action?" *Anticancer research* **1997**, *17*.
- [83] Al-Achi, A.; Boroujerdi, M. "Pharmacokinetics and tissue uptake of doxorubicin associated with erythrocyte-membrane - Erythrocyte-ghosts vs erythrocyte-vesicles." *Drug Development and Industrial Pharmacy* **1990**, *16*, 2199-2219.
- [84] Moorjani, M.; Lejeune, A.; Gicquaud, C.; Lacroix, J.; Poyet, P.; Gaudreault, R. "Nanoerythroosomes, a new derivative of erythrocyte ghost .2. Identification of the mechanism of action." *Anticancer Research* **1996**, *16*, 2831-2836.

- [85] Lejeune, A.; Poyet, P.; Gaudreault, R. C.; Gicquaud, C. "Nanoerythroosomes, a new derivative of erythrocyte ghost .3. Is phagocytosis involved in the mechanism of action?" *Anticancer Research* **1997**, *17*, 3599-3603.
- [86] Desilets, J.; Lejeune, A.; Mercer, J.; Gicquaud, C. "Nanoerythroosomes, a new derivative of erythrocyte ghost: IV. Fate of reinjected nanoerythroosomes." *Anticancer Research* **2001**, *21*, 1741-1747.
- [87] Agnihotri, J.; Gajbhiye, V.; Jain, N. K. "Engineered cellular carrier nanoerythroosomes as potential targeting vectors for anti-malarial drug." *Asian J. Pharm. Asian Journal of Pharmaceutics* **2010**, *4*, 116-120.
- [88] Agnihotri, J.; Jain, N. K. "Biodegradable long circulating cellular carrier for antimalarial drug pyrimethamine." *Artificial Cells Nanomedicine and Biotechnology* **2013**, *41*, 309-314.
- [89] Gupta, N.; Patel, B.; Ahsan, F. "Nano-engineered erythrocyte ghosts as inhalational carriers for delivery of fasudil: Preparation and characterization." *Pharmaceutical Research* **2014**, *31*, 1553-1565.
- [90] Payne, G. F.; Kim, E.; Cheng, Y.; Wu, H.-C.; Ghodssi, R.; Rubloff, G. W.; Raghavan, S. R.; Culver, J. N.; Bentley, W. E. "Accessing biology's toolbox for the mesoscale biofabrication of soft matter." *Soft Matter* **2013**, *9*, 6019.
- [91] Wu, H. C.; Shi, X. W.; Tsao, C. Y.; Lewandowski, A. T.; Fernandes, R.; Hung, C. W.; DeShong, P.; Kobatake, E.; Valdes, J. J.; Payne, G. F.; Bentley, W. E. "Biofabrication of antibodies and antigens via IgG-binding domain engineered with activatable pentatyrosine pro-tag." *Biotechnol Bioeng* **2009**, *103*, 231-40.
- [92] Patel, P. D.; Dand, N.; Hirlekar, R. S.; Kadam, V. J. "Drug loaded erythrocytes: As novel drug delivery system." *Current Pharmaceutical Design* **2008**, *14*, 63-70.
- [93] Mohandas, N.; Gallagher, P. G. "Red cell membrane: past, present, and future." *Blood* **2008**, *112*, 3939-3948.
- [94] D'Arrigo, P.; Servi, S. "Synthesis of lysophospholipids." *Molecules* **2010**, *15*, 1354-77.
- [95] Senavirathna, L. K.; Fernando, R.; Maples, D.; Zheng, Y.; Polf, J. C.; Ranjan, A. "Tumor Spheroids as an in vitro model for determining the therapeutic response to proton beam radiotherapy and thermally sensitive nanocarriers." *Theranostics* **2013**, *3*, 687-91.

- [96] Needham, D.; Park, J. Y.; Wright, A. M.; Tong, J. H. "Materials characterization of the low temperature sensitive liposome (LTSL): effects of the lipid composition (lysolipid and DSPE-PEG2000) on the thermal transition and release of doxorubicin." *Faraday Discussions* **2013**, *161*, 515-534.
- [97] Valen, G.; Sonden, A.; Vaage, J.; Malm, E.; Kjellstrom, B. T. "Hydrogen peroxide induces endothelial cell atypia and cytoskeleton depolymerization." *Free Radical Biology and Medicine* **1999**, *26*, 1480-1488.
- [98] Lin, H. J.; Wang, X. T.; Shaffer, K. M.; Sasaki, C. Y.; Ma, W. "Characterization of H₂O₂-induced acute apoptosis in cultured neural stem/progenitor cells." *Febs Letters* **2004**, *570*, 102-106.